



FACULTY OF ENGINEERING AND SUSTAINABLE DEVELOPMENT

Department of Building, Energy and Environmental Engineering

---

# An experimental study in the near field of a turbulent round free jet

JORGE SORBE

AUGUST, 2014

Student thesis, Master degree (one year), 15 HE  
Energy Systems

Master Programme in Energy Systems

Course 1

Supervisor: Shahriar Ghahremanian  
Examiner: Hans Wigö



## **PREFACE**

Firstly, I must thank my supervisor Shahriar Ghahremanian for giving me the opportunity to work with him and learn a lot during the project duration. Also, to the University of Gävle and the teachers of Master in energy systems for the knowledge contributed during this year. Finally in the university, I want to thank to the director of the master program, Nawzad, for the planning in the master in energy system.

Following, I want to express my gratitude to my family by finance my studies during a long time. Also, to Mirian Rodriguez because she has helped me correcting my English report. And finally, to Jorge Bascuas by his help to me in Matlab program.

At final, I want to dedicate the project in memorial of my aunt Paloma Sorbe.



## ABSTRACT

This work is about the study of the turbulent round jet to low Reynolds number in the outlet of a nozzle due to the countless uses in the industrial field. The objectives of the thesis are the verification of the Particle Image Velocimetry (PIV) data with other methods and authors and the analysis of the near and transition region of the flow.

The method has been divided in three parts: processing of the PIV data that has been the normalization and union of the data; validation of the PIV measurement in comparison with other related studies; and the analysis of the near and intermediate field with the known data.

Once that this part has been realized, the results and the discussion of the same have been presented. The preparation of the data has been made with a big accuracy how it has been demonstrated in the report. The verification of the PIV data has been affirmative with a big similitude for every magnitude that have been compared with other authors.

Several patterns and an equation checked have been obtained in the analysis of the potential and transition region of the turbulent flow. In the near field, a model has been found in the self-similarity turbulence intensity. In the intermediate field, the inverse streamwise mean velocity have been proved that follow a lineal function depending the parameters of the Reynolds number and nozzle geometry. Also, self-similarity streamwise velocity has evolved similar to Gaussian distribution.

Finally, an evaluation of the principal point to eddy will be development has been made. Turbulent kinetic energy and vector fields have demonstrated that vortices are created in the intersection between near and intermediate zone.



# INDEX

1	INTRODUCTION .....	1
1.1	Background.....	1
1.2	Aim .....	2
1.3	Thesis outline.....	2
2	THEORY .....	5
2.1	Turbulent flow .....	5
2.1.1	Definition .....	5
2.1.2	Characteristics of the turbulent flow .....	5
2.1.3	Regions of the flow .....	6
2.1.4	Reynolds number .....	8
2.1.5	Sutherland's law .....	8
2.1.6	Governing equations .....	8
2.2	Discovery in characterization of a turbulent flow .....	10
2.2.1	Mean velocity .....	10
2.2.2	Turbulence intensity.....	13
2.2.3	Reynolds stresses .....	15
2.3	Entrainment.....	16
2.4	Initial condition.....	17
2.4.1	Reynolds number .....	17
2.4.2	Inner-wall nozzle exit .....	18
2.5	Hot-Wire Anemometry (HWA).....	18
2.5.1	Definition .....	18
2.5.2	HWA characteristics .....	20
2.5.3	Governing equations .....	20
2.6	Particle Image Velocimetry (PIV) .....	21
2.6.1	Definition .....	22
2.6.2	Characteristic of PIV system .....	25
2.6.3	Technique of measurement .....	25
2.7	CFD technique .....	27
2.7.1	RANS models .....	28
3	PROCESS .....	31
3.1	Beginning information.....	31
3.2	Processing of the PIV data.....	32
3.3	Validation of the PIV data .....	35
3.4	Analysis of the near zone.....	36

4	RESULTS.....	37
4.1	Processing of the PIV data.....	37
4.2	Validation of the PIV data results.....	50
4.3	Results for the analysis in the near and intermediate fields.....	60
5	DISCUSSION.....	63
5.1	Discussion of the processing of the PIV data .....	63
5.2	Discussion about the validity of the PIV data .....	64
5.3	Discussion of the results for the analysis.....	67
5.4	Strengths and weakness of the work.....	69
6	CONCLUSION .....	71
	REFERENCES .....	73

## TABLE OF CONTENTS

Figure 1.1: Turbulent flow of smoke from a chimney on the left and vortices around an aircraft on the right. ....	1
Figure 2.1: Schematic of a free jet in the axial coordinate [2]. ....	7
Figure 2.2: Schematic of a free jet in the radial coordinates [3]. ....	7
Figure 2.3: Streamwise mean velocity profile at different axial positions and authors [3]. ..	11
Figure 2.4: Normalized radial mean velocity profile in the far field [3]. ....	11
Figure 2.5: Axial decay of centerline mean velocity [3]. ....	12
Figure 2.6: Streamwise and radial turbulence intensity profiles [3]. ....	14
Figure 2.7: Evolution of centerline turbulence intensity [3]. ....	14
Figure 2.8: Reynolds shear stress at different positions [3]. ....	15
Figure 2.9: Hot-wire anemometry apparatus. ....	19
Figure 2.10: Flow data collection of a hot-wire anemometry. ....	19
Figure 2.11: Schematic of a typical PIV experiment. ....	22
Figure 2.12: Procedure of data collection in a PIV system. ....	27
Figure 3.1: The different zones in the inlet PIV data. ....	31
Figure 3.2: Difference area between two curves. ....	34
Figure 3.3: Difference area between two bar function. ....	35
Figure 4.1: Streamwise velocity decay in the centerline for the different zones. ....	38
Figure 4.2: Streamwise turbulence intensity along the centerline for the different zones. ....	38
Figure 4.3: Radial turbulence intensity along the centerline for the different zones. ....	39
Figure 4.4: Streamwise mean velocity profiles in the intersection between zone 1 and 2 for different streamwise axial positions. ....	40
Figure 4.5: Streamwise turbulence intensity profile for several axial positions in the intersection between zone 1 and 2. ....	41
Figure 4.6: Reynolds shear stress XY profile in the intersection between zone 1 and 2 for different axial points. ....	42
Figure 4.7: Streamwise mean velocity profiles in several points in the intersection between zone 1 and 2. ....	43
Figure 4.8: Streamwise turbulence intensity profiles in the intersection between zone 2 and 3. ....	44
Figure 4.9: Reynolds shear stress profiles in the intersection between zone 2 and 3. ....	45
Figure 4.10: Streamwise mean velocity profiles in the intersection between zone 3 and 4. ....	46
Figure 4.11: Streamwise turbulence intensity profiles in the intersection between zone 3 and 4. ....	47
Figure 4.12: Reynolds shear stress profiles in the intersection between zone 3 and 4. ....	48

Figure 4.13: Streamwise mean velocity decay in the centerline for several authors and methods. ....	51
Figure 4.14: Inverse streamwise means velocity in the centerline for PIV data and the linear function approximation for the slope.....	51
Figure 4.15: Streamwise mean velocity profile in several axial points for HWA method (blue) and PIV method (red) for Shahriar data. ....	52
Figure 4.16: Streamwise mean velocity profile in the near field for PIV and Mi et al. studies. ....	53
Figure 4.17: Streamwise turbulence intensity along the centerline normalized by centerline velocity. ....	53
Figure 4.18: Streamwise turbulence intensity along the centerline normalized by maximum velocity. ....	54
Figure 4.19: Streamwise turbulence intensity profiles in the PIV method. ....	55
Figure 4.20: Streamwise turbulence intensity profile in the intermediate field.....	55
Figure 4.21: Radial turbulence intensity along the centerline. ....	56
Figure 4.22: Radial turbulence intensity profile in the intermediate field.....	56
Figure 4.23: Reynolds shear stress profile in the near field. ....	57
Figure 4.24: Reynolds shear stress profile in the intermediate field. ....	57
Figure 4.25: Self-similarity streamwise mean velocity for several method data.....	58
Figure 4.26: Self-similarity streamwise turbulence intensity. ....	59
Figure 4.27: Turbulent kinetic energy along the centerline with Shahriar PIV data. ....	60
Figure 4.28: Turbulent kinetic profile in the out of the nozzle for Shahriar PIV data.....	60
Figure 4.29: Turbulent kinetic energy profile for several points with the PIV method data. ....	61
Figure 4.30: Velocity field for several regions of the flow represented by vectors. ....	62

## TABLES

Table 2.1: Linear slope, linear start abscissa and virtual origin abscissa as a function of the Reynolds number by Todde [17]. .....	13
Table 2.2: Legend of the characteristic graphics of the turbulent flow [3].....	16
Table 2.3: Linear fit constant for equation 2.8 [3]. .....	17
Table 2.4: Types of PIV techniques and brief description of them. ....	24
Table 4.1: Bulk velocity values and the test conditions.....	37
Table 4.2: Difference area results in the intersection between zone 1 and 2. ....	49
Table 4.3: Difference area results in the intersection between zone 2 and 3. ....	49
Table 4.4: Difference area results in the intersection between zone 3 and 4. ....	50
Table 4.5: Turbulence plot features for PIV and Todde [17] experiment measures. ....	54



# 1 INTRODUCTION

In this chapter an introduction of the work will be presented explaining the reasons of why is important the study of this topic, a brief history of the authors who made it before and different methods to measure the jet. Finally the aim of the project will be presented.

## 1.1 *Background*

The study of the turbulent flow is very important as this one is found in a lot of daily activities such as water flow in a river, smoke from a chimney, or vortices around a helicopter or an aircraft (see Fig. 1.1). In industry, it can be found in transport and mix fluid (burner nozzles and fuel injectors). Then, for new industrial designs, it is necessary to predict the round-jet dynamics with three dimensional computational fluid dynamics (CFD).



**Figure 1.1: Turbulent flow of smoke from a chimney on the left and vortices around an aircraft on the right.**

The round turbulent jet has been studied since late 18th century, when Reynolds (1883) examined the transition of the flow from laminar to turbulent. A lot of authors have studied the behavior of the flow in the outlet of a nozzle for different types of jets and regions since 1950s and early 1960s. Some of these authors are Wygnanski and Fiedler, Pachapakesan and Lumley, Hussein et Al, Bogulawski and Popiel, Quinn and Militzer, etc.

The initial attempts to study the turbulence phenomena was limited to single point probe measurements (e.g. pressure probes, hot-wire and laser-Doppler anemometry) and corresponding statistics. Spatial and temporal two point correlations measurements were

also obtained but the interpretation is limited as its averaging nature makes it unable to resolve much of the underlying physics of the flow, Cantwell (1981).

From 1970s the photographic methods were introduced to the flow study with application of lasers to quantify velocity measurements (especially Particle Image Velocimetry (PIV)). PIV method has improved the visualization measurements of the vortex.

## **1.2    *Aim***

This study begins by unknowns mentioned in the review paper by Ball et al. (2012) [3]. In this paper, the mixing transition region is unknown, or only studied in a general way. However, the behavior of the flow in the far field, which is already studied, depends on the mixing transition region.

The interactions among the coherent structures and the mixing transition of a single round jet at a low Reynolds number is going to be studied. Two measurements techniques (Hot-Wire Anemometry and high- speed Particle Image Velocimetry) were used and collected by Shahriar Ghahremanian.

The first aim is to compare the results of these two measurements with previous studies in terms of flow properties. The second aim is to study the evolution of scales and turbulence structures from time-resolved PIV measurements.

The study will contribute with detailed experimental data for a round jet at a low Reynolds number by using a two dimensional time-resolved measurement technique. Moreover, it may be valuable for the validation of numerical models used to compute the flow field of the round jets.

## **1.3    *Thesis outline***

In this chapter, a brief introduction of the turbulent flow, other author studies and measurement methods have been presented. Also it has been explained the aim of the present project and why the performance of this thesis is needed.

Chapter 2 explains the theory that after will be applied in the method. At first, it will be commented the turbulent flow; definition, characteristics, regions, Reynolds number and the governing equations to the flow moving. Later in the same chapter, the different measurements of the flow, the entrainment and the initial conditions will be analyzed and finally, the different type of data that are going to be used will be mentioned.

In chapter 3, the followed method will be explained and commented. The thesis will be divided in different parts to ease the understanding thereof. Also the equations and suppositions that will be used will be explained.

In chapter 4, the results obtained following the previous chapter will be showed. Graphics and numerical results will be exposed.

Chapter 5 will comment and analyze the showed results in the previous chapter. The followed scheme followed will be the same that in the two earlier chapters. Also the strength and weakness will be exposed.

Finally, in chapter 6, the conclusion of the project will be commented basing in the previous chapters. The principal results and conclusion of them will be expanded. Possible continuations of the present work to improve or complete it will be mentioned.



## 2 THEORY

In the present chapter, the turbulent flow will be introduced and its principal characteristics that later will be studied. The different methods to measure the flow will be explained (PIV and HWA) and several model approximations (CFD) will be treated and analyzed (low Re  $\kappa$ - $\epsilon$  and SST  $\kappa$ - $\omega$ ).

### 2.1 *Turbulent flow*

#### 2.1.1 Definition

In a lot of industrial processes, a turbulent flow is generated. To minimize the drop pressure in the pipe outlet, a contracting nozzle is placed and a top-hat velocity profile is produced in the exit pipe, i.e. a laminar flow. Then, the jet is mixed with the ambient and a turbulent flow is generated.

In fluid mechanics, turbulent flow is called to the fluid movements in a chaotic way, where the particles move in a disordered mode and create little eddies along the trajectory of the flow. The study of turbulent flow has evolved over the last century, alongside the evolution of theoretical, experimental, and computational methods [1].

#### 2.1.2 Characteristics of the turbulent flow

Main characteristics of the turbulent flow have been listed and explained in following [2],[3],[5]:

- Irregularity: the flow introduces random phenomena that it is why, it is necessary to use statistic methods.
- Diffusivity: the turbulence produces a big diffusivity and fast mixes of any property or substance in the flow.
- High Reynolds number: the laminar flow is transformed in turbulent flow when its Reynolds number increases. The instabilities of the flow are linked with non-lineal and viscous terms of the Navier-Stokes equations; which are tied to the Reynolds number.

- Dissipation: the turbulence dissipate the energy supply of the principal flow through eddies, i.e. to keep the turbulence is necessary an external energy source.
- Vorticity fluctuations in three-dimensions.

### 2.1.3 Regions of the flow

The round jet is born out of the nozzle, it will expand in the radial direction with downstream distance until the initial momentum is spread very thinly where viscous action will dissipate energy and the jet dies. Round jets are symmetrical around streamwise centerline, i.e. axisymmetric. The information of this part has been obtained in [2], [3], [5] and [8].

The flow velocity can be divided in axial and radial depending on the direction. The axial region can be divided in several zones depending on the velocity characteristics as it is shown in Fig. 2.1.

- Near field: this zone is found in  $0 \leq y/D \leq 7$ , only appears in jets from contraction nozzle. Here, the flow is stable. The velocity characteristics are similar to the jet velocity and it is located in the so called potential core (top-hat profile) and tends to be nearly constant depending on the type of nozzle.
- Intermediate field or transition region: between  $7 \leq y/D \leq 25$ , this is the least studied region of the round free jet. In this region the flow forms a highly anisotropic turbulent structure which depends on the Reynolds number and the nozzle. Both regions, near and intermediate, are the development zone of the jet.
- Far field or fully developed turbulent mixing layer: located from approximately  $y/D \geq 25$ . The shear layer is thin. Analytical solution of the jet is possible due to self-similarity exhibition of mean flow and turbulence structure. Decay of centerline velocity normalized for exit Reynolds number is:

$$\frac{U}{U_0} = constant \left( \frac{d_0}{y - y_p} \right)$$

Where  $d_0$  is the nozzle diameter and  $(y - y_p)$  is the virtual origin of the jet flow and centerline velocity decay constant.

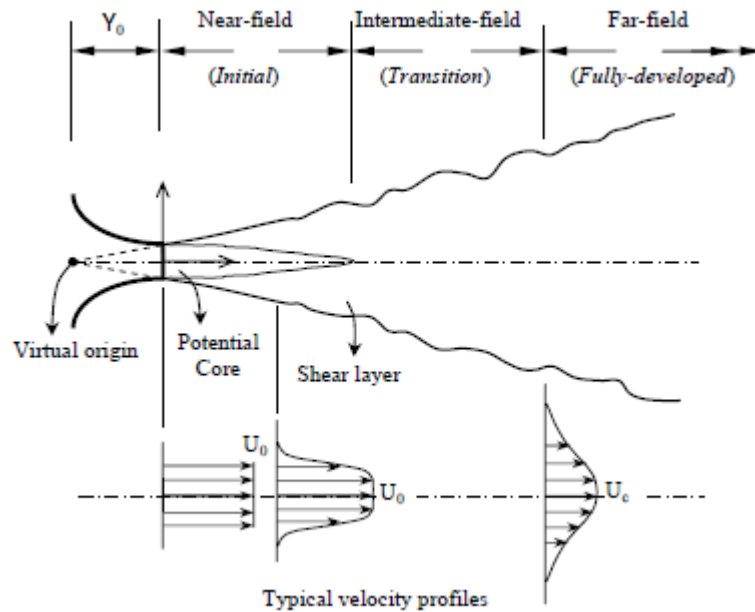


Figure 2.1: Schematic of a free jet in the axial coordinate [2].

In the radial direction, there are three concentric layers, see Fig. 2.2:

- Centerline layer: it is found the maximum axial mean velocity.
- Shear layer: the radial velocity gradient cause vortex cores to form and create large eddies.
- Outer layer: the velocity is approximately tenth of centerline velocity.

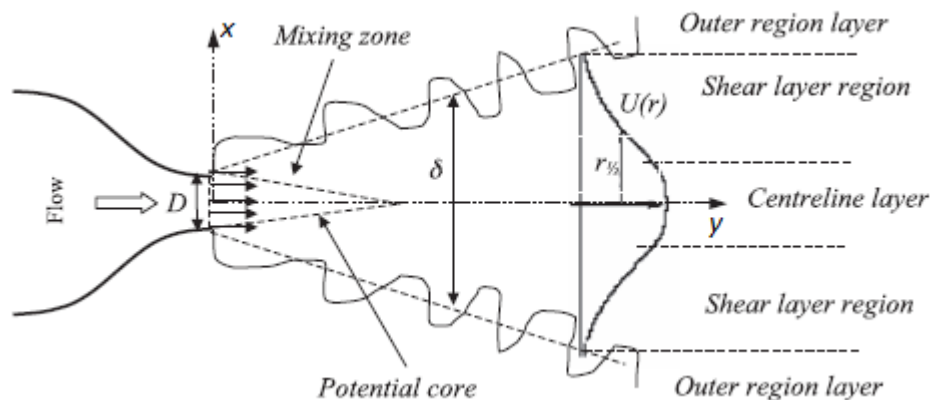


Figure 2.2: Schematic of a free jet in the radial coordinates [3].

### 2.1.4 Reynolds number

Reynolds number is a non-dimensional number that is used to characterize a flow in fluid mechanical. This number was introduced by George Gabriel Stokes, but it was popularized by Osborne Reynolds in 1883. This number characterizes the flow, turbulent or laminar. The definition of the Reynolds number is given by the next equation that is the division between inertial forces and viscosity forces [1].

$$Re = \frac{\rho \cdot U \cdot D}{\mu} = \frac{U \cdot D}{\nu}$$

Where  $\rho$  is the density of the fluid,  $U$  is the velocity of the flow,  $D$  is the diameter of the nozzle,  $\mu$  is the viscosity of this one and  $\nu$  is the kinetic viscosity.

### 2.1.5 Sutherland's law

This law is based on kinetic theory of ideal gas and will be used for calculate the bulk velocity. The Sutherland's law permits to obtain the dynamic viscosity ( $\mu$ ) [15].

$$\mu = \mu_{ref} \cdot \left( \frac{T}{T_{ref}} \right)^{\frac{2}{3}} \cdot \frac{T_{ref} + S}{T + S}$$

Where  $S$  is the Sutherland temperature (k) and for the air its value is 110,4 k.  $T$  and  $T_{ref}$  are the temperature and reference temperature respectively.

In order to calculate the bulk value, the Reynolds number equation has to be applied.

### 2.1.6 Governing equations

The equations that represent the movement of a flow, both laminar and turbulent, are called continuity and Navier-Stokes equations. The unknowns of these equations are the velocity field  $u(x, t)$  and the pressure field  $p(x, t)$  [5], [7].

### 2.1.6.1 Continuity equation

This equation is obtained from the mass conservation rule. This condition is that the change in the mass of the volume is equilibrated with the flow through the superficies of the volume.

$$\frac{d}{dt} \int_V \rho(x, t) dV = - \int_{\delta V} \rho(x, t) \vec{u}(x, t) d\vec{S} = - \int_V \vec{\nabla}(\rho \cdot \vec{u}) dV$$

Where V is the volume and  $\delta V$  is the area of the volume.

If Gauss theorem is applied to this equation and it is supposed steady-state and incompressible fluid:

$$\frac{\partial U_i}{\partial x_j} = 0 \quad or \quad \nabla \cdot \vec{u} = 0$$

### 2.1.6.2 Navier-Stokes equations

These equations are obtained from the Newton's second law, where the time variation of the momentum is equal to the sum of the strengths in the volume.

$$\frac{d}{dt} \int_V \rho \cdot \vec{u} \cdot dV = - \int_{\delta V} \rho(x, t) dS + \int_V B(x, t) dV + \int_{\delta V} \sigma(x, t) dS$$

The first component of the strength is the pressure applied in the volume superficies. The second term is the body forces and finally the third component is the strength due to the internal stresses ( $\sigma$  = stress tensor).

Supposing that air is an ideal gas, steady-state, three dimensional and incompressible, and applying the divergence theorem, Navier-Stokes equation is obtained:

$$\frac{\partial(U_j U_i)}{\partial x_j} = - \frac{1}{\rho} \frac{\partial P}{\partial x_i} + \frac{\partial}{\partial x_j} \left( \nu \frac{\partial P}{\partial x_j} - \overline{u'_i u'_j} \right)$$

## **2.2 *Discovery in characterization of a turbulent flow***

The discovery began in the late 1950s and early 1960s. The principal leader in this field 60 years ago not only was Laurence, but also Ricou and Spalding, and Wygnanski and Fiedler. The need to predict analytically the measurements and characterization of the flow field from a round jet was the goal that drove the investigators to make these studies.

After 1960, David et al. used a single hot-wire anemometer to investigate the near field. A similar relationship with the first distance of the flow jet was demonstrated.

Sami et al. investigated experimentally the near field using both Pitot-static probes and hot-wire anemometers. In this experiment, results showed that the root-mean-square pressure and Reynolds shear stress profile were similar in the near field.

Wygnanski and Fiedler were two of the most influential investigators on the round jet. They made an experimental work and later they presented profiles for mean velocity, energy balance, second and third order single point correlations and length scales. Years later, Hussein et al. and Capp et al. examined the accuracy of these measurements. In order to do it, two velocimetry techniques were used, hot wire and laser Doppler anemometry techniques. Capp et al. found high discrepancies between the two techniques. Hussein et al. compensated these divergences using a flying hot wire. Panchapakesan and Lumley confirmed the conclusions.

George discovered in a theoretical analysis that turbulent jet flow can become asymptotic to a variety of self-similar states, by the initial conditions. Mi et al. examined the theory of George for two jets and affirmed it [3].

The legend of the figures that are going to be presented in this section is explained in table 2.2 at the end of the present chapter.

### **2.2.1 Mean velocity**

The axial mean velocity profile represents the velocity in a point of the downstream flow normalized by the center velocity in each profile, see figure 2.3. The profile is symmetric in the radial direction. It can be seen how the velocity is expanded in the

radial direction downstream. Hrycak et al. studied that the nominal potential core length is largely independent in the turbulent flow of Reynolds number.

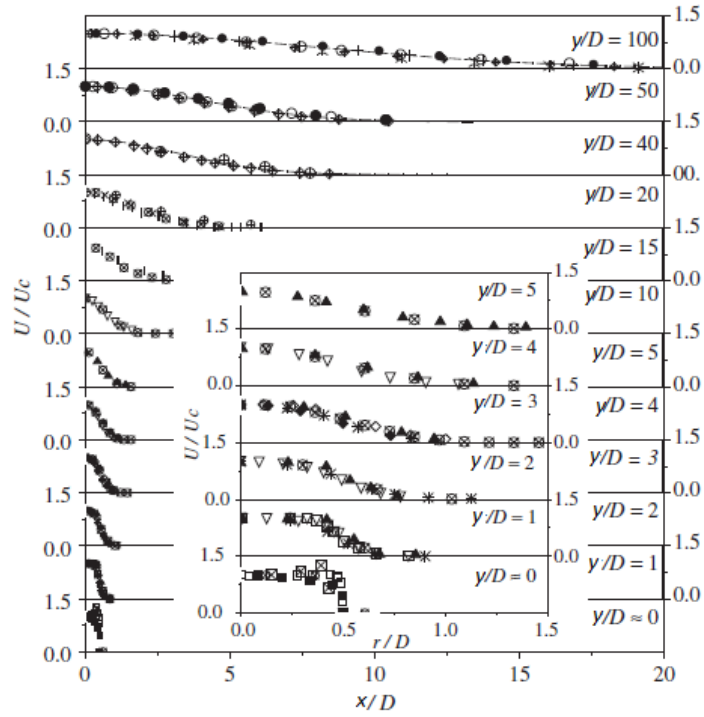


Figure 2.3: Streamwise mean velocity profile at different axial positions and authors [3].

Radial mean velocity profile is the component of the velocity in the radial direction. This one increases the area of the flow. In Fig 2.4, it can be seen the profile normalized with the centerline axial mean velocity in the far field. This velocity is also symmetric around the jet centerline. The flow near to the centerline expands outward, while surrounding fluid retracts laterally inwards.

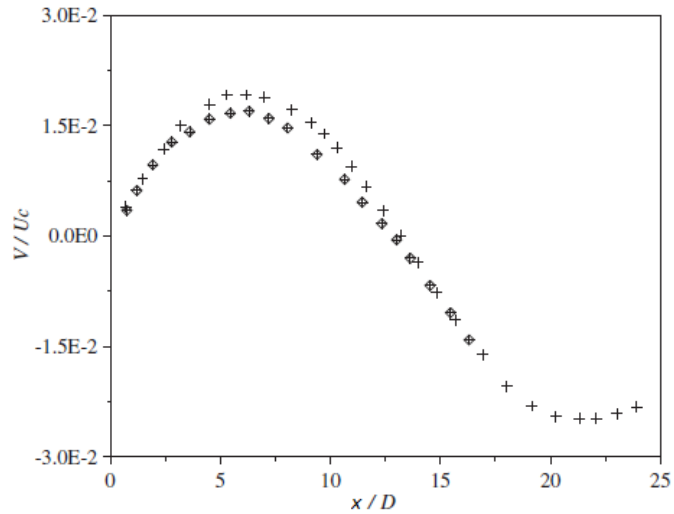
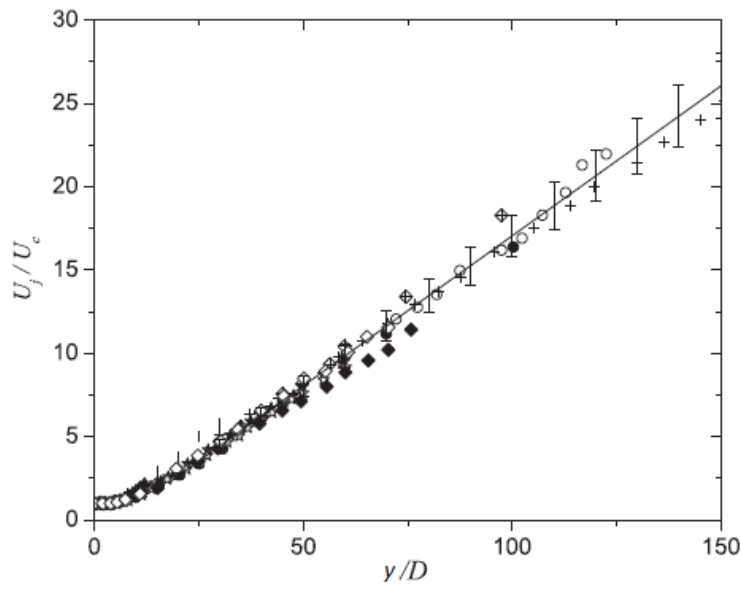


Figure 2.4: Normalized radial mean velocity profile in the far field [3].

The centerline axial mean velocity is shown in figure 2.5. In the graphic it can be seen that the decay of the velocity is linear in the longitudinal distance. In the self-similar region, the decay of the centerline mean velocity is given by the following equation:

$$\frac{U_j}{U_c} = \frac{1}{B} \left( \frac{x}{D} - \frac{x_0}{D} \right)$$

Where  $x_0$  is the virtual origin,  $D$  is the nozzle diameter and  $B$  is the constant of decay.



**Figure 2.5: Axial decay of centerline mean velocity [3].**

Values of other author to compare the inverse of the streamwise mean velocity data are presented in table 2.1 [17].

**Table 2.1: Linear slope, linear start abscissa and virtual origin abscissa as a function of the Reynolds number by Todde [17].**

Exit section nominal $Re_D$ [-]	Linear slope [-]	Start of lin. [ $x/D$ ]	Virtual Orig. [ $X_p/D$ ]
850	0.2417	11.50	6.0594
1050	0.2418	9.50	4.1725
1350	0.2471	8.00	2.9632
1620	0.2471	7.50	2.5287
2175	0.2156	7.00	1.5188
2700	0.2147	7.00	1.4366
4050	0.2156	7.25	1.4523
5400	0.2111	8.00	1.5241
6750	0.2011	8.50	1.5873

### 2.2.2 Turbulence intensity

The turbulence intensity is caused by the turbulence effect or the eddy existence. This measurement is not exactly as it is based on statistic methods. In order to obtain this value, firstly, it is necessary to calculate the instant value of the velocity in the time and the mean. Once these calculations are obtained, it will be possible to calculate the fluctuant velocity.

$$u' = u - U \quad ; \quad v' = v - V$$

Where  $u$  and  $v$  are the total streamwise and radial velocity respectively; and  $U$  and  $V$  are the components of the streamwise and radial mean velocity.

Then, in order to obtain the turbulence intensity normalized, it is necessary to divide the fluctuant velocity already calculated by the centerline velocity.

In fig. 2.6 and 2.7, it can be seen the axial ( $u'/U_c$ ) and radial ( $v'/U_c$ ) turbulence intensity normalized by the centerline mean velocity. In the first figure shows the profiles and the second the evolution in the centerline downstream. Generally, the radial turbulence intensity is lower than the axial one in the stream wise direction, that is due to the larger structures that appears in the principal flow direction and the turbulence field cannot be assumed isotropic.

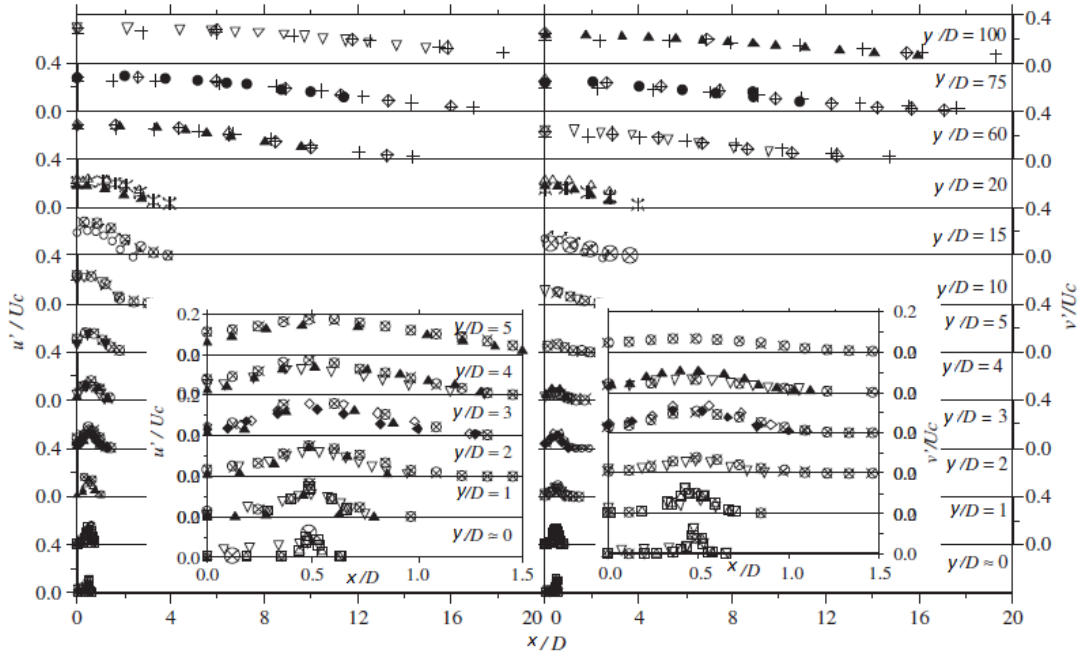


Figure 2.6: Streamwise and radial turbulence intensity profiles [3].

The longitudinal evolution of the turbulence intensities along the centerline ( $x/D = 0$ ) is represented in figure 2.7. In the first zone, the near field, the turbulence intensity increases with a high slope, due to the large scale coherent motions that appear in the shear layer. In the far field, it is constant. It is observed that axial intensity achieves the maximum point before than radial turbulence intensity being the maximum point of the axial intensity higher than the radial one. Once this maximum point is achieved, it can be seen that the turbulence intensity remain constant.

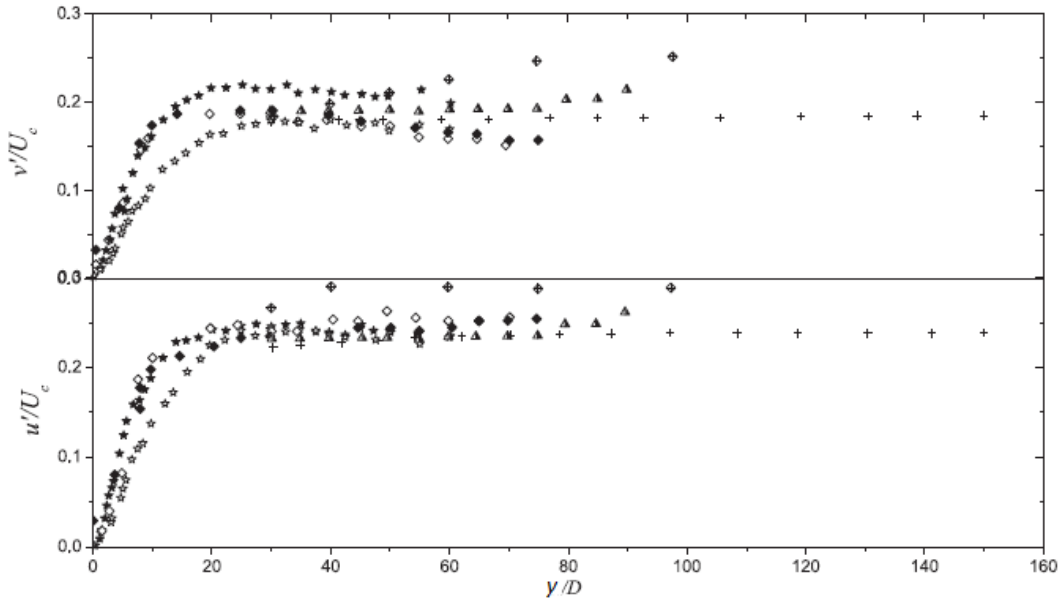


Figure 2.7: Evolution of centerline turbulence intensity [3].

### 2.2.3 Reynolds stresses

Reynolds shear stresses are normalized by centerline velocity's square which is represented in figure 2.8. The maximum value of these profiles moves away of the centerline with downstream distance. This occurs as the maximum momentum is in the jet shear layer.

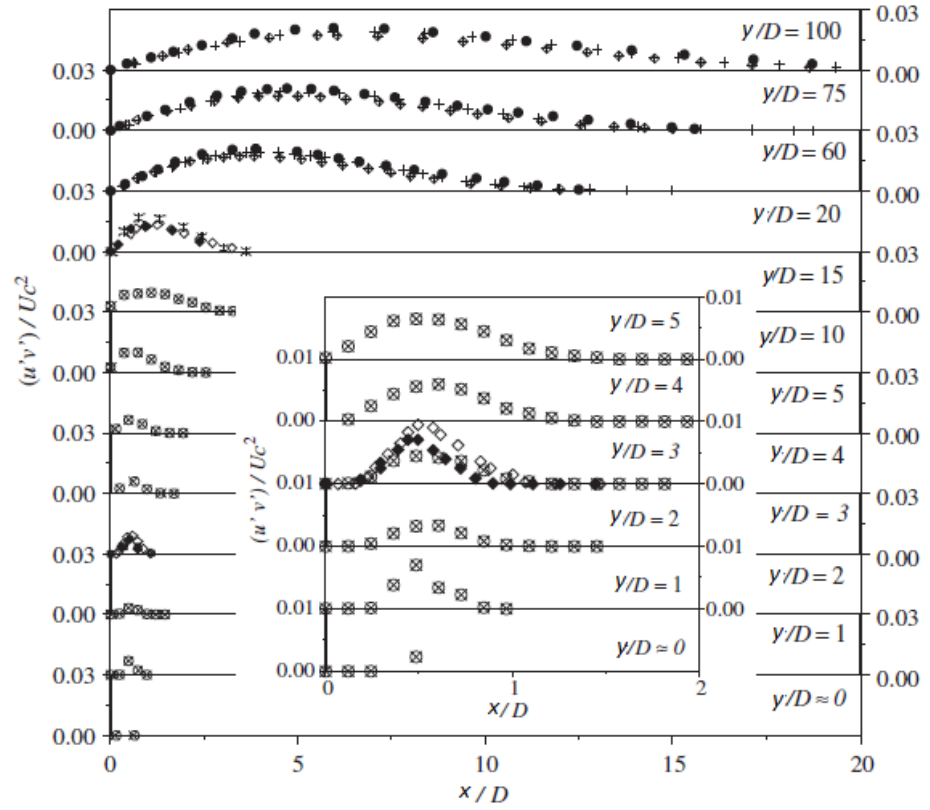



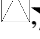











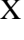


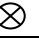


Figure 2.8: Reynolds shear stress at different positions [3].

**Table 2.2: Legend of the characteristic graphics of the turbulent flow [3].**

Symbol	Author
	Wyganski and Fiedler
	Boguslawski and Popiel
	Quinn and Militzer, contraction nozzle
	Quinn and Militzer, sharp nozzle
	Panchapakesan and Lumley
	Hussein et al.; single hot wire
	Hussein et al.; laser Doppler anemometry
	Abdel-Rahman et al.
	Weisgraber and Liepmann
	Mi et al.; contraction nozzle
	Mi et al.; pipe nozzle
	Mi et al.; orifice nozzle
	Romano
	Xu and Antonia; contraction nozzle
	Xu and Antonia; pipe nozzle
	Gamard et al.
	Kwon and Seo
	Iqbal and Thomas
	Fellouah and Pollard

## 2.3 Entrainment

Entrainment is the introduction of the surrounding irrational flow in the turbulent jet trough the boundary. It keeps the momentum flow rate stable and increases the mass flow rate in the same way that the flow is moved away from the inlet nozzle; [3], [6] and [8].

In order to analyze this parameter, measurements of the jet half- radius growth are used. Entrainment increases linearly downstream following the potential core. Furthermore, the next equation approximates the half- radius ( $r_{1/2}$ ) for values that fulfill the following condition:  $x/D \geq 15$ .

$$\frac{r_{1/2}}{D} = A \cdot \frac{x}{D} - B$$

Some investigators obtained values for the parameters, A and B, as it can be seen in table 2.3.

**Table 2.3: Linear fit constant for equation 2.8 [3].**

Author	Nozzle	A	B
Panchapakesan and Lumley	Contraction	0,096	
Xu and Antonia	Contraction	0,095	
	Pipe jet	0,086	
Fellouah and Pollard	Contraction	0,097	0,259

## 2.4 Initial condition

Along the history, a lot of investigators have seen the existence of a strong dependence between the initial conditions and the development of the flow, both near field and far field. The principal effects that change the flow's development are the Reynolds number and the nozzle characteristics [3] [7].

### 2.4.1 Reynolds number

The Reynolds number reliance with the round jet has been studied in the turbulent flow field in order to understand the development of this one. Gilbrech (1991) observed that when Reynolds number increased the mixing rate was also higher in the far field. Koochesfahani and Dimotakis (1986) saw a rapid mixing transition for the same behavior of the Reynolds number. Panchapakesan and Lumley (1993) and Hussein et al. (1994) checked that Reynolds number was independent to the normalized mean velocity profile and spreading rate for low Reynolds number values. Hollingsworth (1989) affirmed that these theories were correct for Reynolds number values lower than 10000. Dimotakis (2000) found that for Reynolds higher than 25000, entrainment rates follow an asymptotic behavior.

## 2.4.2 Inner-wall nozzle exit

Initial velocity profiles of the turbulent flow are depended of the nozzle exit, in relation to several characteristics of this one. Mi and Nathan (2004) concluded that centerline mean velocity increased with a contoured nozzle and a long pipe. Moreover, an increase of the vortex was observed with a smoothly contoured nozzle.

The most important characteristics of the nozzle that modify the configuration of the jet are the smoothly contoured nozzle, sharp-edged orifice and the pipe flow configuration.

## 2.5 *Hot-Wire Anemometry (HWA)*

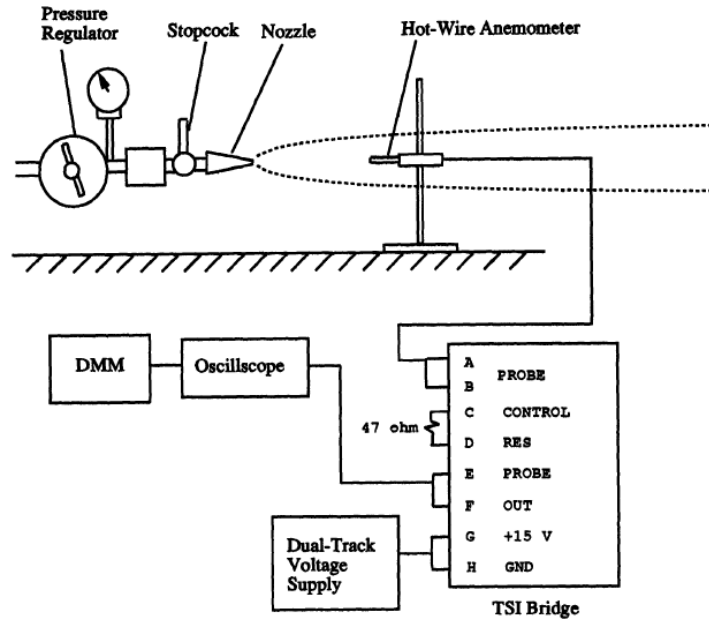
An anemometer is a device that is used to measure the wind. There are two types of anemometer, the first one measures the velocity of the wind and the second one the pressure. These two variables are directly related to an equation, then, if one of the magnitudes is known, the other is also known.

The HWA is a type of anemometer, Boussinesq (1905) was one of the first investigators of this technique. He studied the heat transfer from a heated wire. Dryden and Knethe (1929) were the first to measure quantitatively the fluctuations in subsonic incompressible flows with a constant current anemometry. Ziegler (1934) developed constant temperature anemometer. Finally, Kovasznay (1950's) extended HWA to compressible flows and developed a graphical technique to obtain the data. Nowadays, several improvements have been made in this device to improve the quality of the measurements.

All the information presented in this section has been obtained from the following references: [9][10].

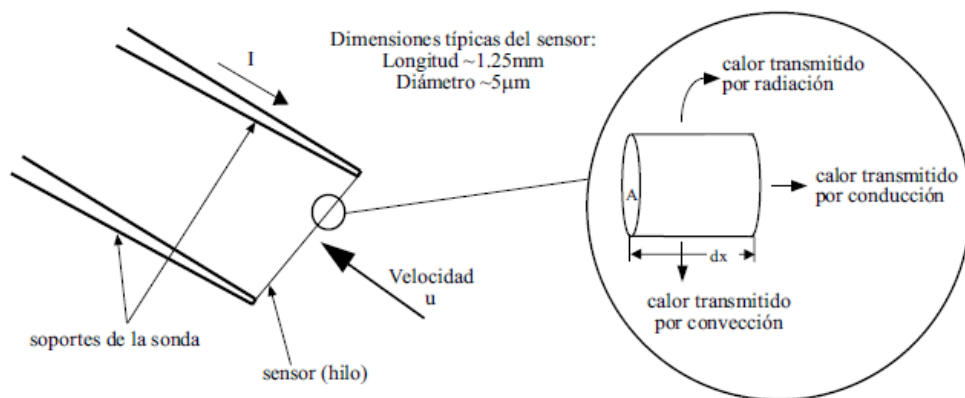
### 2.5.1 Definition

The hot-wire anemometry is an apparatus that measures the instantaneous velocity and temperature of a flow, see figure 2.9. It is ideal for velocity fluctuations and turbulent flows. It exist two type of HWA, constant current anemometer (CCA) and constant temperature anemometer (CTA).



**Figure 2.9: Hot-wire anemometry apparatus.**

The heat-wire anemometry measurement technique is based in the heat transfer from a heated wire to the surrounding fluid. It uses a little metal wire how detecting element. This wire is cooled by the fluid by conduction; forced and free convection; and radiation. The drop in the temperature of the wire produces a decreased in the electrical resistance of the wire. Then, it is possible to know the transfer energy and so the velocity of the flow. A HWA is represented in figure 2.10. It will be explained more detailed in governing equations of HWA.



**Figure 2.10: Flow data collection of a hot-wire anemometry.**

The environment of the process does not interfere in the development of the experiment, that is why accurate data will likely be obtained. In order to do it, the work zone has to be clearly defined and studied.

### 2.5.2 HWA characteristics

This device is normally used to calculate the velocity vector field of the turbulent flow, due to its characteristics that are suitable for this type of jet. Some of the most relevant advantages and drawbacks are:

- Its small size allows having a lower disturbance in the flow, although the device contaminates flow and modifies it slightly.
- Capturing the velocity fluctuation with accuracy is possible due to the high frequency response and sensitivity.
- The velocities obtained from hot-wire anemometry are wide range because the device is accuracy.
- In economic terms, this one is low in cost in comparison with others similar devices.
- HWA is good apparatus to calculate the velocity field in a line, for calculate the velocity field in 2-D, a lot of hot-wire anemometers are necessary and the flow can be modified severely.

### 2.5.3 Governing equations

The governing equations to obtain the velocity of the flow are related to a heat balance that takes place in the hot-wire anemometry. Moreover, thermal energy stored in wire (E) is equal to difference between power generated by Joule heating (W) and heat transfer to surrounding (H). The energy balance links these terms in the next equation.

$$\frac{dE}{dt} = W - H$$

For equilibrium conditions the heat storage is null and then the Joule heating power is equal to convective heat transfer.

$$\frac{dE}{dt} = 0 \Rightarrow W = H$$

With this energy balance simplified, it is possible to calculate the velocity of the flow ( $v_f$ ).

$$\begin{cases} W = H \\ W = I^2 \cdot R_w \\ H = h \cdot A_w \cdot (T_w - T_a) \end{cases}$$

$$I^2 \cdot R_w = h \cdot A_w \cdot (T_w - T_a) \Rightarrow h = a + b \cdot v_f^c \Rightarrow v_f$$

Where  $I$  is the current,  $R_w$  the resistance of the wire and the temperature variation is the difference between wire and ambient temperature. The film coefficient of heat transfer is called  $h$ .  $a$ ,  $b$  and  $n$  are data of calibration.

## 2.6 Particle Image Velocimetry (PIV)

In general, the information in this chapter has been obtained in several sources that have been referenced by [11], [12], [13] and [14].

Particle image velocimetry is a non-intrusive optical method that has been used the last three decades, due to the improvement in the devices that this technique requires how cameras, lasers and computers. Also, several PIV techniques have been invented to improve the flow study.

The first investigators in this technique were Barker and Fournery (1977), Dudderar and Simpkins (1977) and Grousson and Mallick (1977). They demonstrated that was possible to apply the method of laser speckle, then used in solid mechanics, to measure the velocity field.

Meynart (1983) applied the laser speckle method in laminar and turbulent flows, demonstrating that it worked in liquids and gases. He referred to this method laser speckle velocimetry (LSV), although often, individual particles appeared in the images, besides speckles.

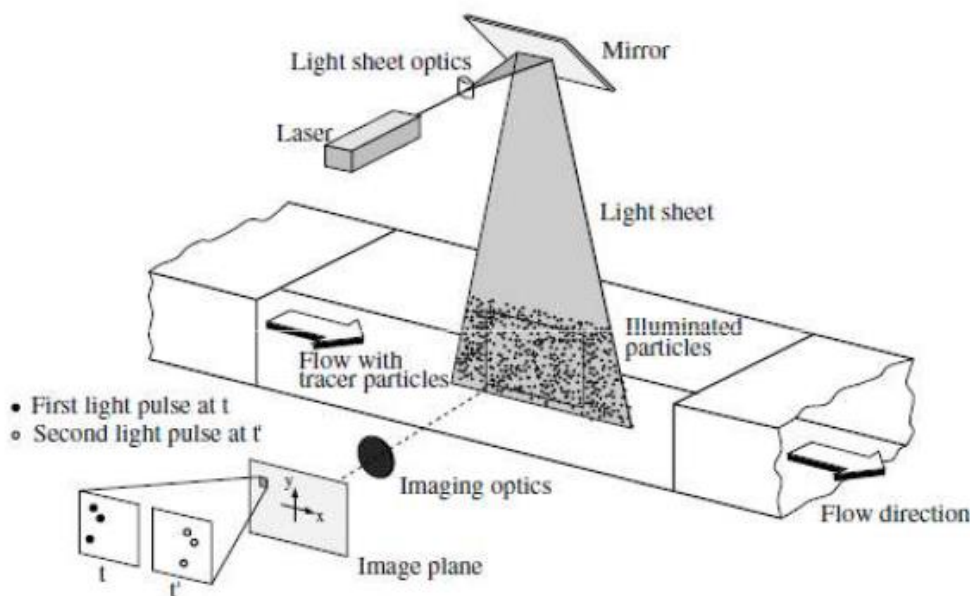
Pickering and Halliwell (1984) and Adrian (1984) discovered that to see the particles in the images, it was necessary to illuminate the particles with a light sheet, and

then speckles and particles could be watched. They named this method particle image velocimetry (PIV).

A lot of researchers studied the PIV method because it offered a promising advance in the investigation of the turbulent flow structure. Search more and more specific of the flow study, it has forced to improve the PIV process. A high intensity illumination was necessary to can capture smaller particles, pulsed lasers were installed to record the finest particles without blurring, and cameras and interrogation by correlation have been linked to record the images. Nowadays, many projects are making to follow improving this promising method.

### 2.6.1 Definition

Particle image velocimetry (PIV) is an optical method of flow visualization used in education and research. It is used to obtain instantaneous velocity measurements and related properties in fluids. The fluid is seeded with tracer particles which, for sufficiently small particles, are assumed to faithfully follow the flow dynamics (the degree to which the particles faithfully follow the flow is represented by the Stokes number). The fluid with entrained particles is illuminated so that particles are visible, a schematic of the installation can seeing in figure 2.11. The motion of the seeding particles is used to calculate speed and direction (the velocity field) of the flow being studied [1].



**Figure 2.11: Schematic of a typical PIV experiment.**

PIV method has improved in the last 30 years and then different PIVs methods have been development. Traditional PIV provides two velocity components in 2D plane and these velocities allow calculating four velocity gradient. Out of plane vorticity and three strain rate tensor are obtained. Assuming isotropic approximations, kinetic energy dissipation rate can be calculated with one velocity gradient.

Following with two-dimensional methods, for time resolved PIV, two acceleration components are obtained due to high speed recording system, and from these one, dissipation rate turbulence is calculated. Stereoscopic PIV technique provides out-of-plane velocity components also, and so the six velocity gradient tensor and an accuracy kinetic energy. Dual-plane stereoscopic PIV system allows calculating the full nine velocity gradient components and dynamic properties.

Later three dimensional studies have been invented. Time-resolved stereoscopic PIV system achieve this propose with Taylor's frozen hypothesis that get a quasi-instantaneous reconstruction of the vertical structure in the 3Ds. Time resolved scanning PIV method is used to measure in turbulent flow with low Reynolds number. Time-resolve stereoscopic scanning PIV system is the most complete technique, it is used to study small-scales of turbulence.

In table 2.4, PIV's types are exposed and the parameters that is possible to calculate with each system.

**Table 2.4: Types of PIV techniques and brief description of them.**

Technique	Observation area	Velocity components	Velocity gradient components	Acceleration components	Dynamics properties
Traditional PIV	2D plane	$u, v$	$\frac{\partial u}{\partial x}, \frac{\partial v}{\partial x}$ $\frac{\partial u}{\partial y}, \frac{\partial v}{\partial y}$		$\omega_z$ $\varepsilon_{xx}, \varepsilon_{yy}$ $\varepsilon_{xy}$
Time-resolved PIV	2D plane	$u, v$	$\frac{\partial u}{\partial x}, \frac{\partial v}{\partial x}$ $\frac{\partial u}{\partial y}, \frac{\partial v}{\partial y}$	$\frac{\partial u}{\partial t}, \frac{\partial v}{\partial t}$	$\omega_z$ $\varepsilon_{xx}, \varepsilon_{yy}$ $\varepsilon_{xy}$
Stereoscopic PIV	2D plane	$u, v, w$	$\frac{\partial u}{\partial x}, \frac{\partial v}{\partial x}, \frac{\partial w}{\partial x}$ $\frac{\partial u}{\partial y}, \frac{\partial v}{\partial y}, \frac{\partial w}{\partial y}$		$\omega_z$ $\varepsilon_{xx}, \varepsilon_{yy}, \varepsilon_{zz}$ $\varepsilon_{xy}$
Dual-plane stereoscopic PIV	Two 2D planes	$u, v, w$	$\frac{\partial u}{\partial x}, \frac{\partial v}{\partial x}, \frac{\partial w}{\partial x}$ $\frac{\partial u}{\partial y}, \frac{\partial v}{\partial y}, \frac{\partial w}{\partial y}$ $\frac{\partial u}{\partial z}, \frac{\partial v}{\partial z}, \frac{\partial w}{\partial z}$		$\omega_x, \omega_y, \omega_z$ $\varepsilon_{xx}, \varepsilon_{yy}, \varepsilon_{zz}$ $\varepsilon_{xy}, \varepsilon_{yz}, \varepsilon_{zx}$ $1/2\omega_i\omega_i$ $\omega_i\varepsilon_{ij}\omega_i$ $2v\varepsilon_{ij}\varepsilon_{ij}$
Time-resolved stereoscopic PIV	Quasi-instantaneous 3D volume	$u, v, w$	$\frac{\partial u}{\partial x}, \frac{\partial v}{\partial x}, \frac{\partial w}{\partial x}$ $\frac{\partial u}{\partial y}, \frac{\partial v}{\partial y}, \frac{\partial w}{\partial y}$ $\frac{\partial u}{\partial z}, \frac{\partial v}{\partial z}, \frac{\partial w}{\partial z}$		$\omega_x, \omega_y, \omega_z$ $\varepsilon_{xx}, \varepsilon_{yy}, \varepsilon_{zz}$ $\varepsilon_{xy}, \varepsilon_{yz}, \varepsilon_{zx}$ $1/2\omega_i\omega_i$ $\omega_i\varepsilon_{ij}\omega_i$ $2v\varepsilon_{ij}\varepsilon_{ij}$
Time-resolved scanning PIV	3D volume	$u, v, w$	$\frac{\partial u}{\partial x}, \frac{\partial v}{\partial x}$ $\frac{\partial u}{\partial y}, \frac{\partial v}{\partial y}$ $\frac{\partial u}{\partial z}, \frac{\partial v}{\partial z}$	$\frac{\partial u}{\partial t}, \frac{\partial v}{\partial t}$	$\omega_z$ $\varepsilon_{xx}, \varepsilon_{yy}$ $\varepsilon_{xy}$
Time-resolved stereoscopic scanning PIV	3D volume	$u, v, w$	$\frac{\partial u}{\partial x}, \frac{\partial v}{\partial x}, \frac{\partial w}{\partial x}$ $\frac{\partial u}{\partial y}, \frac{\partial v}{\partial y}, \frac{\partial w}{\partial y}$ $\frac{\partial u}{\partial z}, \frac{\partial v}{\partial z}, \frac{\partial w}{\partial z}$	$\frac{\partial u}{\partial t}, \frac{\partial v}{\partial t}, \frac{\partial w}{\partial t}$	$\omega_x, \omega_y, \omega_z$ $\varepsilon_{xx}, \varepsilon_{yy}, \varepsilon_{zz}$ $\varepsilon_{xy}, \varepsilon_{yz}, \varepsilon_{zx}$ $1/2\omega_i\omega_i$ $\omega_i\varepsilon_{ij}\omega_i$ $2v\varepsilon_{ij}\varepsilon_{ij}$

## 2.6.2 Characteristic of PIV system

Some of the main properties of PIV technique and why it is good system to study the turbulent flow are in the next points.

- Non-instructive technique is maybe the most important characteristic of this method, due to the non-modification of the jet.
- The velocity of the flow is measured indirectly through the tracer particles within the flow.
- PIV permits extract information out of large parts of the flow through an image.
- It is necessary to investigate in the tracer particles for velocity lag does not exist. Small tracer particles follow more accuracy the jet.
- If the particles are smaller, for example in a gas fluid is necessary more intensity light.
- The duration of the pulse.
- Time delay between pulses has to be enough long to can measure the particle displacement between the images. And enough short to the particles does not leave the illumine zone.
- A homogeneous particle distribution permits an optimal evaluation.

## 2.6.3 Technique of measurement

In order to measure the velocity field of the flow, the velocity of the tracer particles is obtained and it is supposed that the velocity flow is the equal to this one. That is why the particles selection is a fundamental part of the experiment and the tracer particles movement have to be the most similar possible to the flow movement as the accuracy of the results depends on this similarity.

To calculate the velocity field, a slim light sheet is pulsed in the cross-section of the flow to illuminate the tracer particles by a laser. Then with a photographic or electronic medium (digital camera) an image of the tracer particle in the jet is recorded in data base. To calculate the field velocity, the image has to be recorded at least for two times in a known time interval ( $\Delta t$ ) to obtain the two positions of each particle and then the displacement of it ( $\Delta x$ ). The instantaneous velocity can be calculated from this parameters ( $U(x,t)$ ).

$$\vec{U}(\vec{x}, t) = \frac{\Delta \vec{x}}{\Delta t}$$

Although it seems easy, there are a lot of variables in the practice that make the data collection really difficult and imprecise if it is made in a wrong way. The more relevant aspects in the PIV method are the following and it can be seen in figure 2.12.

- Tracer particles: in order to obtain accurate results in the practice, it is necessary that the particles follow the flow the most similar way to the original fluid. They disperse enough light so that the images can be recorded. Finally, to obtain a uniform distribution, the particles quantity is important.
- Lighting system: a short pulse and slim plane of the light has to be goaled for the best results.
- Recording system: CCD digital cameras are normally used, due to its good quality of the image.
- Analysis of the image: correlations are employed to calculate the displacement of the particles in two consecutive images. Once it is obtained, the velocity of the field can be calculated.
- After-process: finally other magnitudes are calculated depending of the after work and the method errors are represented to know the reliability of the technique.

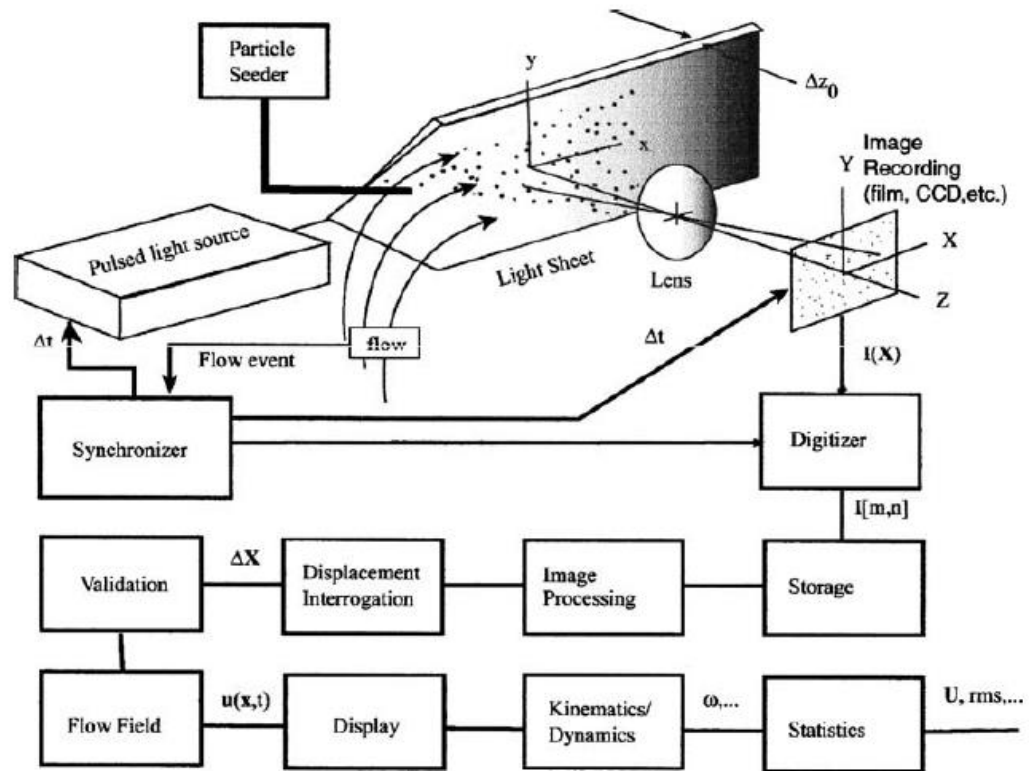


Figure 2.12: Procedure of data collection in a PIV system.

## 2.7 CFD technique

This chapter is based in the following references [20], [16], [21] and [22].

New industrial designs need to predict the flow development to optimize the process. Then it is necessary some method to foretell it. It can be done by experimental or computational methods. The experimental methods can be more accurate, but the problem is that they are more expensive and slower than computational methods. Moreover experimental methods only work for single purpose and with scale models. Finally, CFD can obtain unlimited number of points in the system, that does not occur for experimental methods.

Computational Fluid Dynamics (CFD) is a branch of fluid mechanics that uses numerical methods and algorithms to solve and analyze problems that involve fluid flows. Computers are used to perform the calculations required to simulate the interaction of liquids and gases with surfaces defined by boundary conditions. With high-speed supercomputers, better solutions can be achieved. Ongoing research yields software that

improves the accuracy and speed of complex simulation scenarios such as transonic or turbulent flows [1].

It exist several CFD models to predict the turbulent flow depending of the governing equations that they are based. Some of them are explained in the next list.

- Direct Number Simulation (DNS): it solves the Navier-Stokes equations directly. It is very accuracy, but the computational cost is high.
- Large Eddy Simulation (LES): this method is based in resolve big scales of fluid model the little ones.
- Reynolds Average Navier-Stokes (RANS): it calculates the Reynolds equations that are the average Navier-Stokes equations.
- Detached Eddy Simulation (DES): it is a hybrid method between RANS and LES.

### 2.7.1 RANS models

This model is often used for engineering applications because of its low computational cost and its acceptable approximation to the turbulent flow development. The system is based in the Navier-Stokes equations previously explained. In this approximation Reynolds stress is approached applying Boussinesq hypothesis.

$$-\overline{u_i' u_j'} = \nu_t \left( \frac{\partial u_i}{\partial x_j} + \frac{\partial u_j}{\partial x_i} \right) - \frac{2}{3} \left( k + \nu_t \frac{\partial u_k}{\partial x_k} \right) \delta_{ij}$$

A general way for the turbulence model equation is next expressed, where there are two additional transport equations for turbulent kinetic energy (k) and turbulence dissipation rate ( $\epsilon$ ) or specific dissipation rate ( $\omega$ ). Moreover turbulent viscosity ( $\nu_t$ ) is assumed isotropic quantity.

$$\frac{\partial \bar{\Phi}}{\partial t} + \bar{u}_j \frac{\partial \bar{\Phi}}{\partial x_j} - \frac{\partial}{\partial x_j} \left( \Gamma_{\Phi, eff} \frac{\partial \bar{\Phi}}{\partial x_j} \right) = S_{\Phi}$$

Where  $\Phi$  is the variables,  $\Gamma_{\Phi, eff}$  is the effective diffusion coefficient and  $S_{\Phi}$  represents the source term.

#### 2.7.1.1 Low Re k- $\epsilon$ model

The Low Reynolds k- $\epsilon$  model solves for two variables: k; the turbulent kinetic energy, and  $\epsilon$ ; the rate of dissipation of kinetic energy. This model doesn't use wall conditions, then the flow is simulated everywhere. The k- $\epsilon$  model is very popular for industrial applications due to its good convergence rate and relatively low memory requirements, more than simply k- $\epsilon$  model (it does not very accurately compute flow fields that exhibit adverse pressure gradients, strong curvature to the flow, or jet flow). Low Re k- $\epsilon$  model not use wall functions, lift and drag forces and heat flux can be modeled with higher accuracy.

#### 2.7.1.2 SST k- $\omega$

Finally, the SST model is a combination of the k-epsilon in the free stream and the k-omega models near the walls. It does not use wall functions and tends to be most accurate when solving the flow near the wall. The SST model does not always converge to the solution quickly, so the k-epsilon or k-omega models are often solved first to give good initial conditions. In an example model, the SST model solves for flow over a NACA 0012 Airfoil, and the results are shown to correctly compare with experimental data.



### 3 PROCESS

In this chapter, the method used to perform the present project is going to be explained. This thesis has been divided in three different parts that are: the treatment of the PIV data, validation of these values and then examination of the near zone in the turbulent flow.

#### 3.1 *Beginning information*

For the collection data in the PIV method, the study area is going to be divided in four different zones that measure approximately eight times the diameter of the nozzle (see figure 3.1). The different zones will have an intersection area that will be necessary to split up.

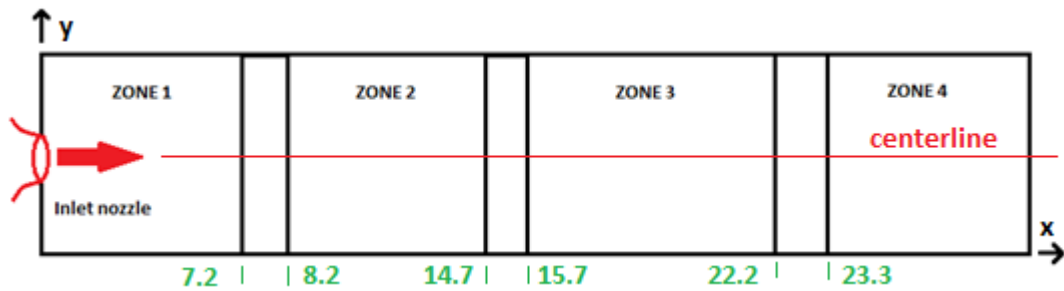


Figure 3.1: The different zones in the inlet PIV data.

Several magnitudes are going to be obtained of the PIV method by Shahriar Ghahremanian, which are the average velocity in the two dimensions, the length of average velocity, the average kinetic energy, the root mean square velocity in the two dimensions, the length of root mean square velocity, the mean turbulent kinetic energy, the Reynolds stress (XX, YY and XY) and the maximum turbulence shear stress.

Each magnitude will be supplied with its coordinates in a “.txt” document with its unit measurement. For each zone the experiment conditions are going to be given, the Reynolds number, the temperature, the pressure, the humidity and the frequency.

### 3.2 Processing of the PIV data

The goal of this section will be obtaining the PIV data in an exclusive zone, i.e. all the zones will be connected in the most similar point of each intersection of the zones.

For this part, excel program will be used to manipulate the values of the PIV method. Then, the first operation will be copying all data to excel file and ordering it.

The following step will be standardizing the magnitudes to join the different zones. In order to do it, calculating the bulk velocity ( $U_b$ ) will be necessary using the Sutherland's law and Reynolds equation (see theory). Then, all the velocity magnitudes will be divided by bulk velocity and the stresses by the square velocity, depending of the unit measurement of the magnitude.

Firstly, with the Reynolds equation, the velocity has been obtained:

$$Re = \frac{\rho \cdot U \cdot D}{\mu} \rightarrow U = \frac{Re \cdot \mu}{\rho \cdot D}$$

The Reynolds number (Re) is an initial condition of the experiment and its value for all of them is 3290. The diameter (D) is the diameter of the nozzle and the datum is also constant,  $D = 5,8 \text{ mm}$ .

The dynamic viscosity is dependent of the temperature of the test, and it is calculated with the Sutherland's law:

$$\mu = \mu_{ref} \cdot \left( \frac{T}{T_{ref}} \right)^{3/2} \cdot \frac{T_{ref} + S}{T + S}$$

Where reference dynamic viscosity ( $\mu_{ref}$ ) is  $1,71 \cdot 10^{-5} \text{ (m}^2/\text{s)}$ . The reference temperature ( $T_{ref}$ ) is 0 (K) and the Sutherlands constant is 110,4 (K). The temperature (T) is varied in each experiment.

The density ( $\rho$ ) is obtained of the next equation and is dependent of the temperature (T), the humidity (H) and the saturation pressure ( $P_{sat}$ ).

$$\rho = \frac{100 \cdot P_{static}}{M_{air} \cdot T} + \frac{H \cdot P_{sat}}{100 \cdot T} \cdot \left( \frac{1}{M_{vap}} - \frac{1}{M_{air}} \right)$$

Where molar mass dry air ( $M_{air}$ ) is 287,058 (J/kg·K) and molar mass vapor ( $M_{vap}$ ) is 461,523 (J/kg·K).

The saturation pressure is dependent of the test temperature (T) how is expressed in the next equation:

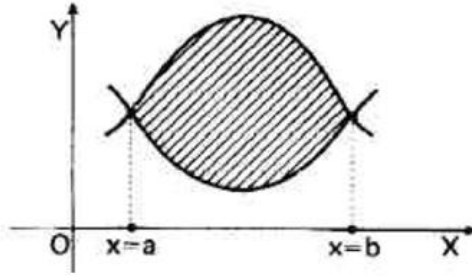
$$P_{sat} = 611 \cdot e^{\frac{17,27 \cdot T}{T+237,3}}$$

Once the standard magnitudes will be calculated, the link of the different zones will be possible. In order to do it, two different methods to find the most similar point in the intersection zone will be used; the calculation of the area difference in all the points and magnitudes, and compare visually the difference between the graphics.

The graphics will not provide a good difference between different points, due to little differences are difficult to distinguish visually. In this comparative method all the magnitudes will be compared, as centerline decay and in different points of the profiles. This graphics will be:

- Axial decay of the centerline mean velocity (U).
- Streamwise mean velocity profiles (U).
- Normalized radial mean velocity profiles (V).
- Evolution of the centerline turbulence intensity (for streamwise and radial) (RMS U and RMS V respectively).
- Radial turbulence intensity profiles (RMS V).
- Streamwise turbulence intensity profiles (RMS U).
- Reynolds shear stresses profiles for the three components ( $u'u'$ ,  $v'v'$  and  $u'v'$ ).

The difference area is a numerical method that provides the difference area between two linear graphics (see figure 3.2). It will be realized for all the profiles that will be possible, the two velocities, the two root mean square velocities and the three Reynolds shear stresses. For all of them, the area will be calculated for each profile and then all the areas will be added. Then the minimum value will be the most similar point between the two consecutive zones.

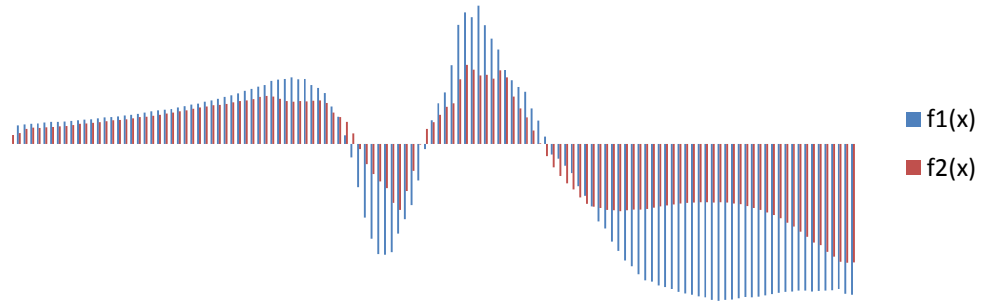


$$s = \left| \int_a^b (f(x) - g(x)) dx \right|$$

**Figure 3.2: Difference area between two curves.**

The difference between areas has been calculated proportionally with the next formula in the case of the project data. In order to do it, two bar functions how in the figure 3.3 have been considered. The area is the integral between the beginning and the ending points for the difference of the functions. Then it can be possible to say that it is equal to the difference between the areas and each area is similar to the sum of each bar area. This area is the multiplication between the height and the thickness for each bar. Finally if the thickness of all the bars is the same the area will be proportional if the thickness is not considered.

$$\begin{aligned}
 A &= \int_a^b (f_1(x) - f_2(x)) dx = \int_a^b f_1(x) dx - \int_a^b f_2(x) dx = A_1 - A_2 \\
 &\approx \sum_1^n (y_n \cdot thickness)_{zone\ 1} - \sum_1^n (y_n \cdot thickness)_{zone\ 2} \\
 &= \left[ \sum_1^n (y_n)_{zone\ 1} - \sum_1^n (y_n)_{zone\ 2} \right] \cdot thickness \\
 &\propto \left[ \sum_1^n (y_n)_{zone\ 1} - \sum_1^n (y_n)_{zone\ 2} \right]
 \end{aligned}$$



**Figure 3.3: Difference area between two bar function.**

### **3.3 Validation of the PIV data**

In this section the data will be compared with others authors values obtained by different methods, in order to check that the PIV values are correct. The divergences and similarities will be analyzed and commented making references to other studies or to the logic. A lot of magnitudes will be compared.

- Streamwise mean velocity decay in the centerline ( $U$ ).
- Streamwise mean velocity profiles ( $V$ ).
- Streamwise turbulence intensity decay in the centerline ( $RMS\ U$ ).
- Streamwise turbulence intensity profiles ( $RMS\ U$ ).
- Radial turbulence intensity decay in the centerline ( $RMS\ V$ ).
- Radial turbulence intensity profiles ( $RMS\ V$ ).
- Reynolds shear stress profiles ( $u'v'$ ).
- Self-similarity for streamwise mean velocity and streamwise turbulence intensity.

### **3.4    *Analysis of the near zone***

An interpretation of the PIV data will be made in this part of the project to obtain more information of the turbulent flow in the near and intermediate zone. In order to do it, several magnitudes and different graphics will be presented and examined.

- Turbulent kinetic energy decay in the centerline and profiles (TKE).
- Vector field for streamwise mean velocity.
- Self-similarity graphics.
- Others graphics of the previous section that will be relevant.

## 4 RESULTS

In this section an exposition of the principal results is made following the scheme of the process chapter. Several graphics and numerical results will be presented and it will be commented in the next section.

### 4.1 Processing of the PIV data

This part of the project starts when the data of PIV method are obtained and the measurement conditions are known. Then all the values have been introduced in excel program to ease its manipulation.

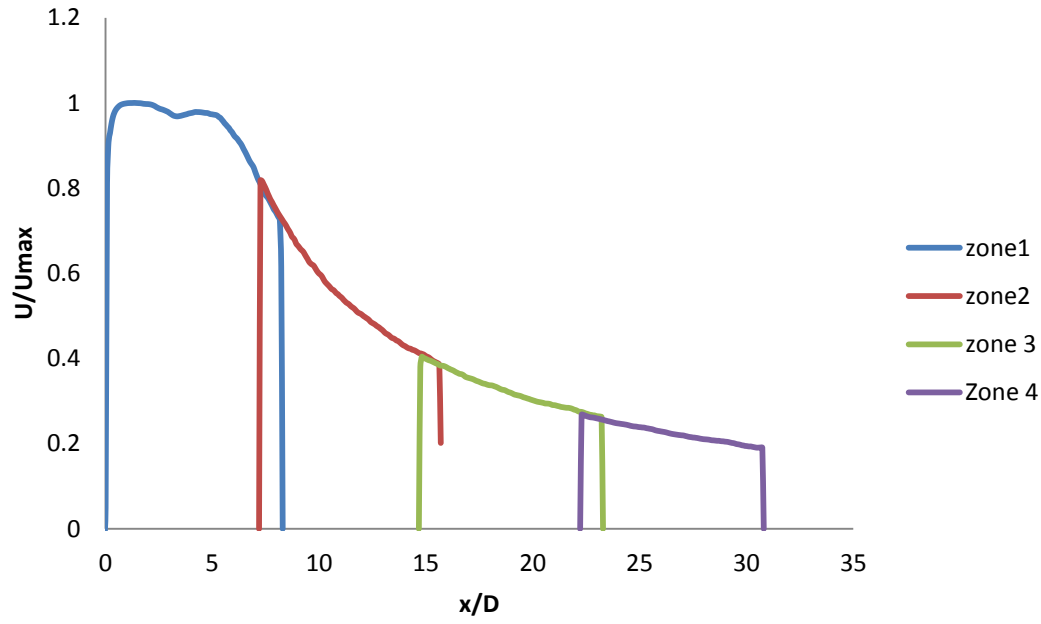
The bulk velocity values and the distinct condition data of each zone measurement are showed in table 4.1.

**Table 4.1: Bulk velocity values and the test conditions.**

	Temperature (°C)	Pressure (mbar)	Humidity (%)	Bulk velocity (m/sec)
Zone 1	22	1010	37	8,67
Zone 2	22	1009	38	8,68
Zone 3	22	1008	41	8,69
Zone 4	23	1012	32	8,71

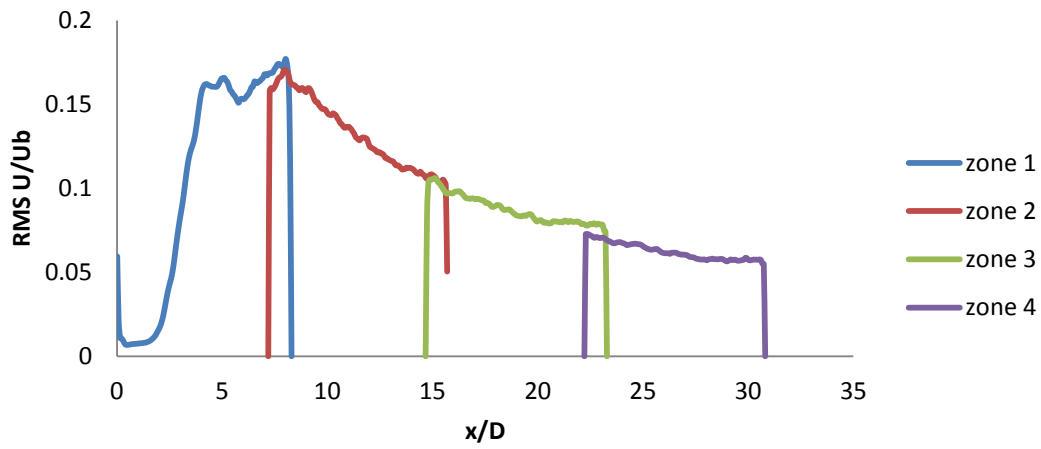
To link the different zones it has been necessary to non-dimension the magnitudes with the bulk velocity. The velocity has been dimensioned dividing by bulk velocity and the stresses dividing by square bulk velocity.

The most representative graphics to find the best points to link the contiguous zones are represented in the next figures. The first graphics and maybe the most representative for including all the zones in the same graphic is the streamwise velocity in the centerline normalized by the maximum velocity value ( $U_{\max}$ ) (see figure 4.1).

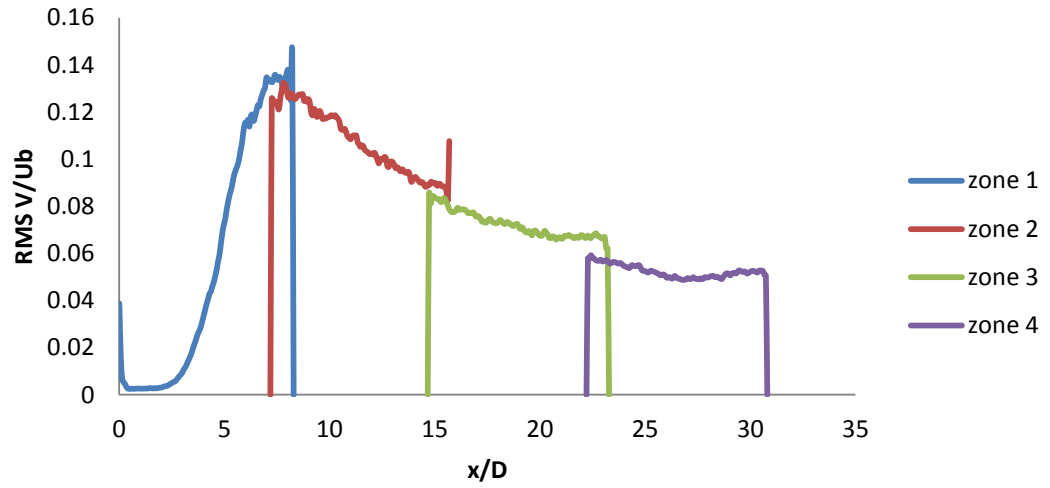


**Figure 4.1: Streamwise velocity decay in the centerline for the different zones.**

Others evolutions of the centerline are the streamwise and the radial turbulence intensities normalized by bulk velocity (see figures 4.2 and 4.3).



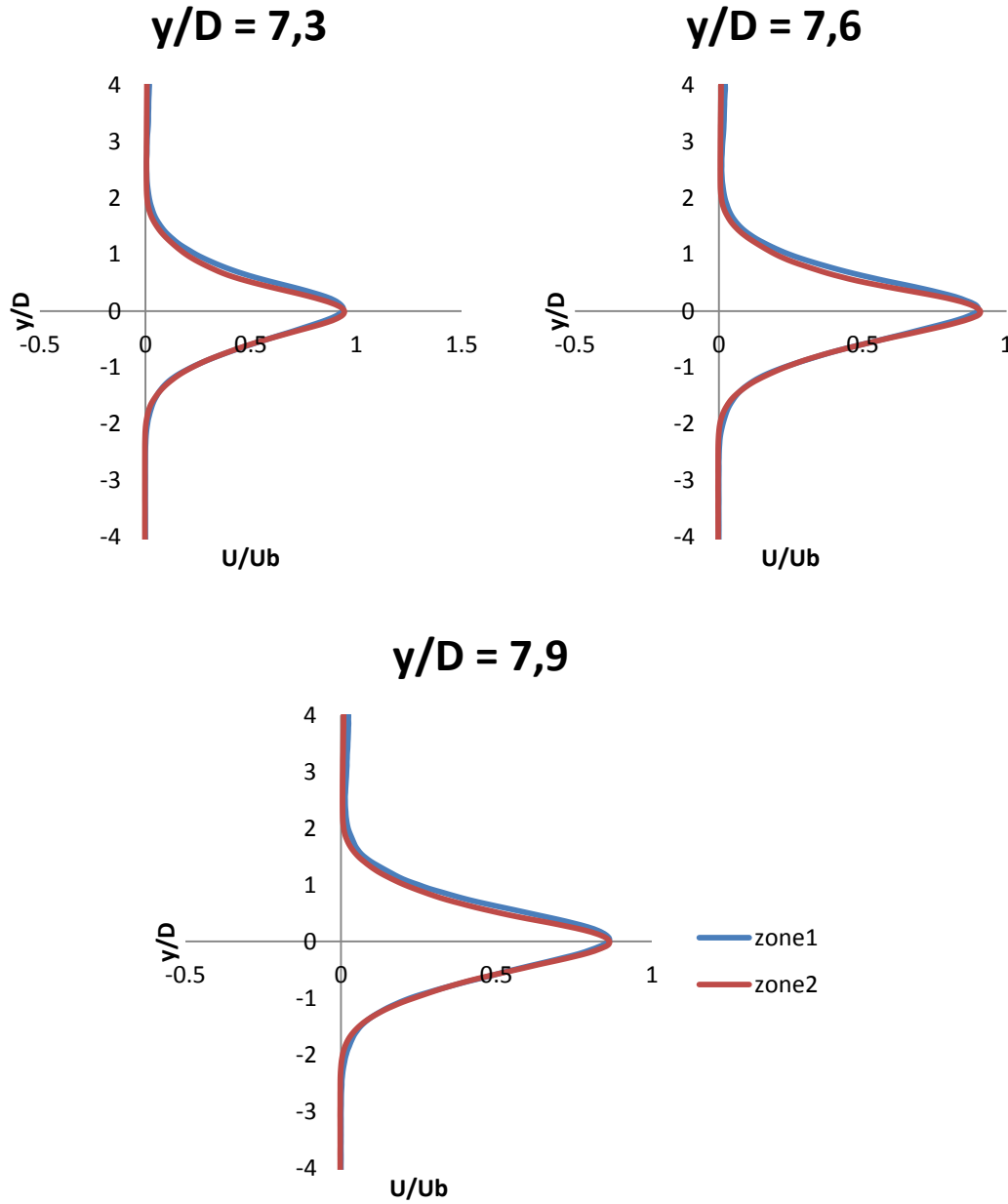
**Figure 4.2: Streamwise turbulence intensity along the centerline for the different zones.**



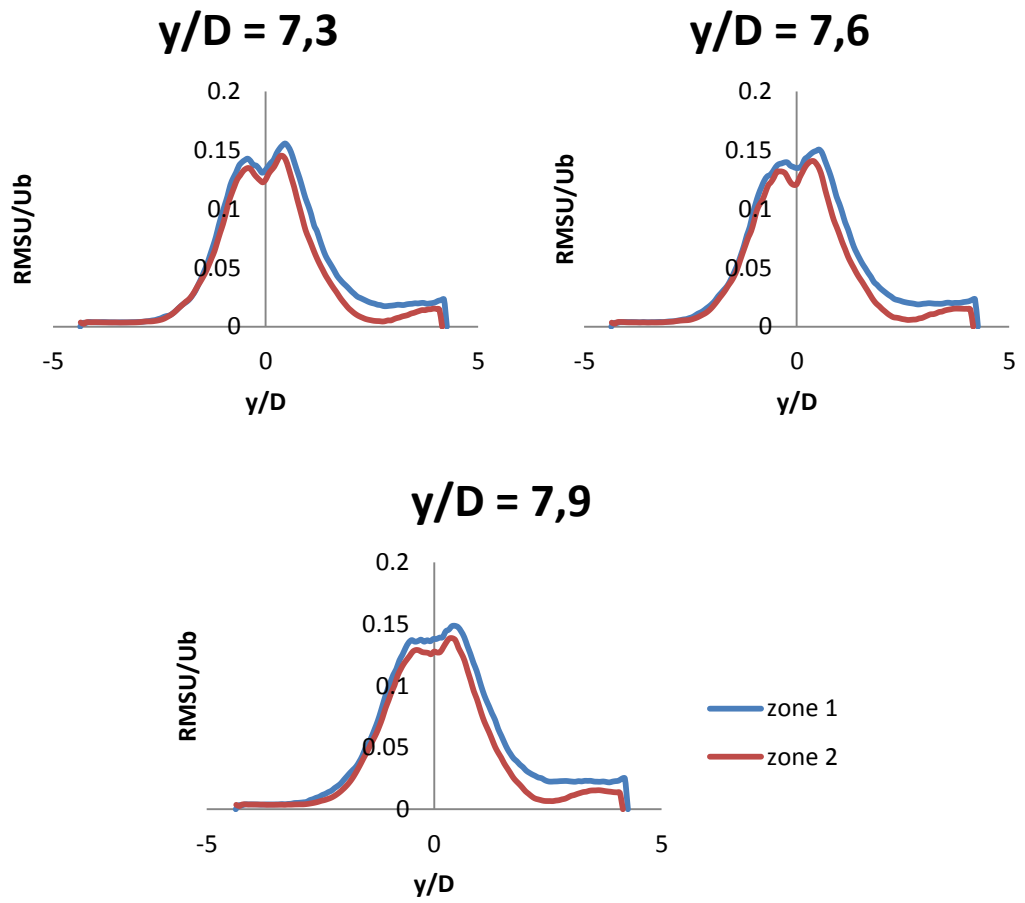
**Figure 4.3: Radial turbulence intensity along the centerline for the different zones.**

Also the profiles of all the magnitudes of the PIV data have been represented. Some of the most representative profiles for different points and intersection zones along the streamwise axis have been exposed in the next figures, all of them have been standardized by the bulk velocity.

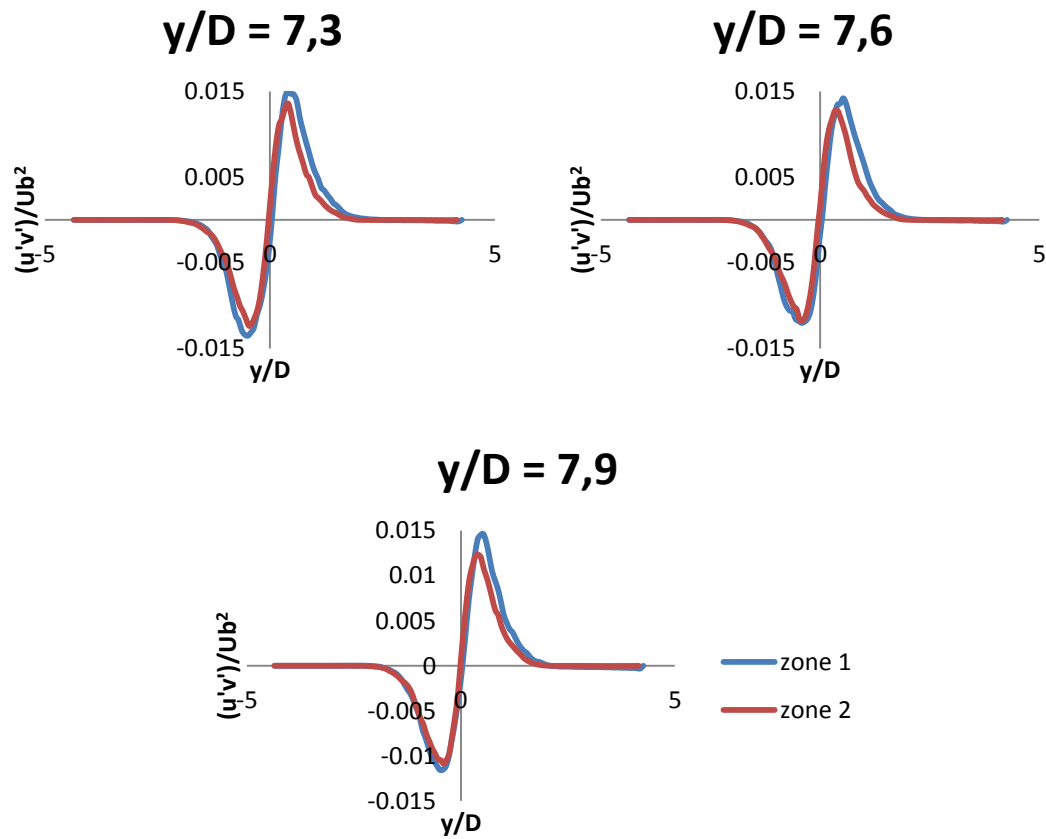
Firstly, in the intersection between zone 1 and 2, streamwise mean velocity, streamwise turbulence velocity and Reynolds shear stress profiles are showed in figures 4.4, 4.5 and 4.6.



**Figure 4.4: Streamwise mean velocity profiles in the intersection between zone 1 and 2 for different streamwise axial positions.**



**Figure 4.5: Streamwise turbulence intensity profile for several axial positions in the intersection between zone 1 and 2.**



**Figure 4.6: Reynolds shear stress XY profile in the intersection between zone 1 and 2 for different axial points.**

Secondly, the same magnitudes are represented for the junction between zone 2 and 3 in the next figures (see figure 4.7, 4.8 and 4.9).

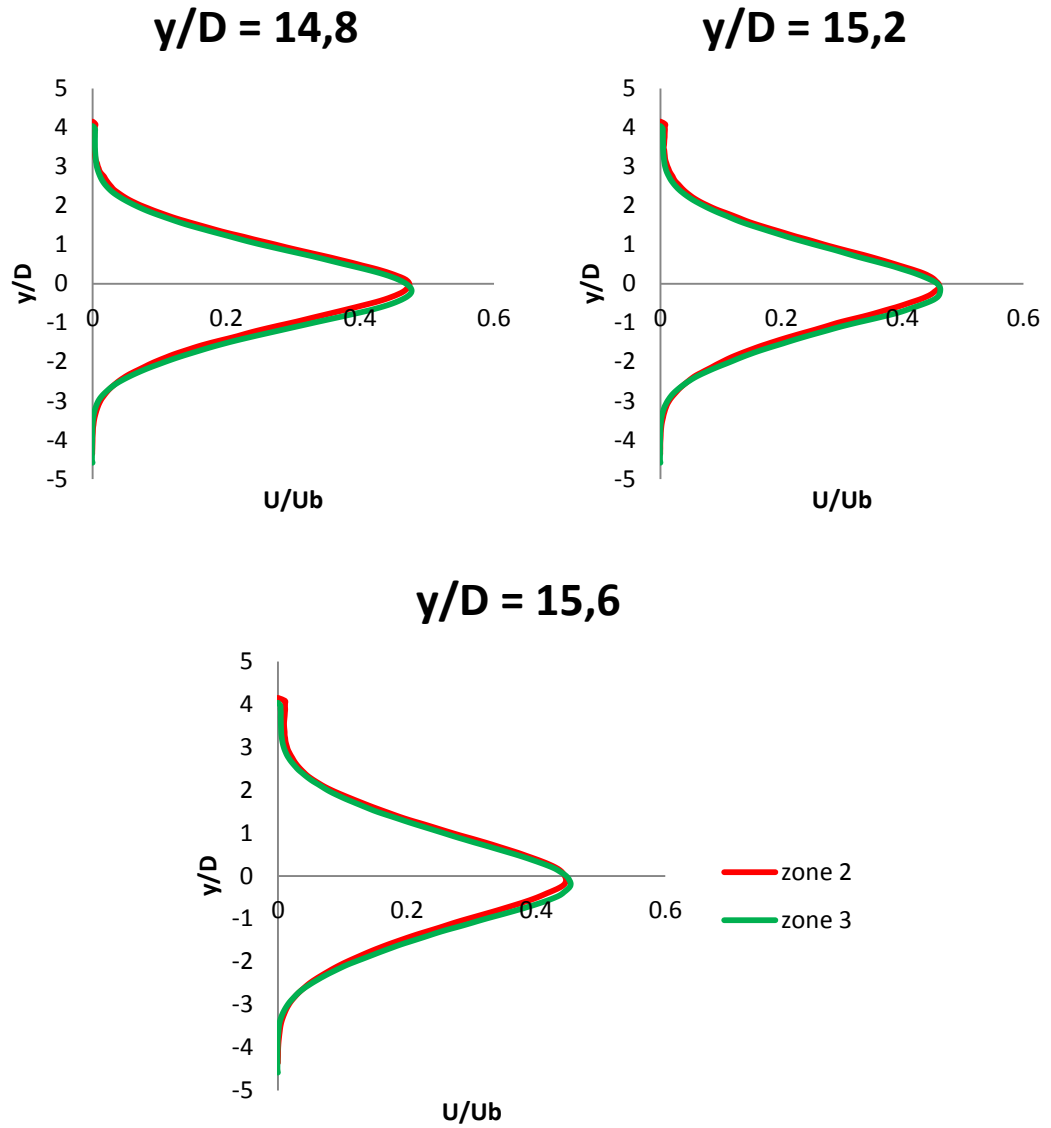


Figure 4.7: Streamwise mean velocity profiles in several points in the intersection between zone 1 and 2.

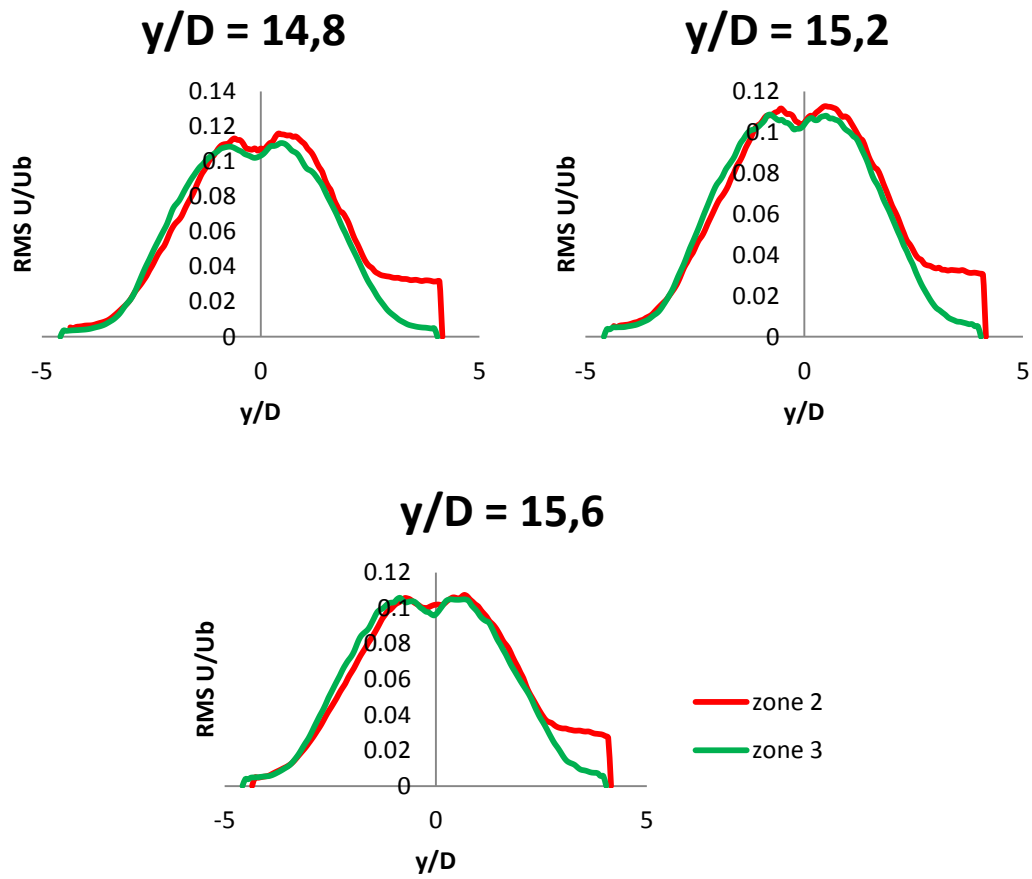


Figure 4.8: Streamwise turbulence intensity profiles in the intersection between zone 2 and 3.

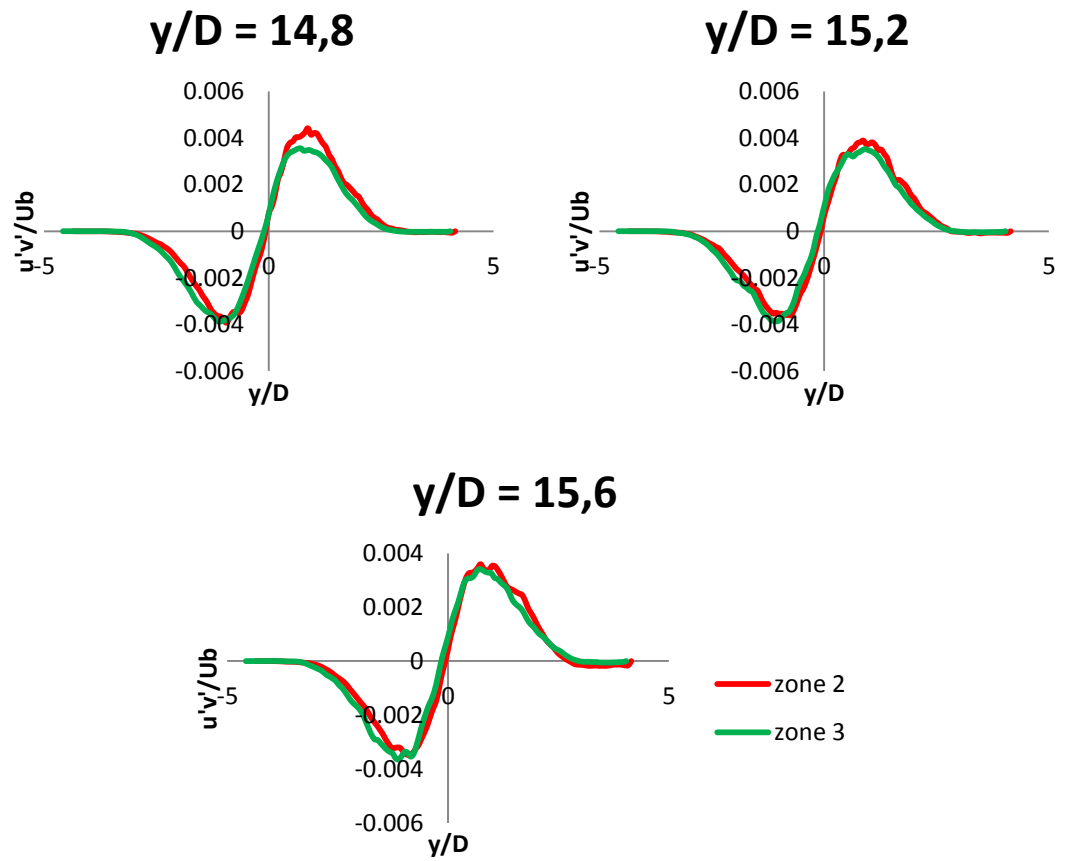
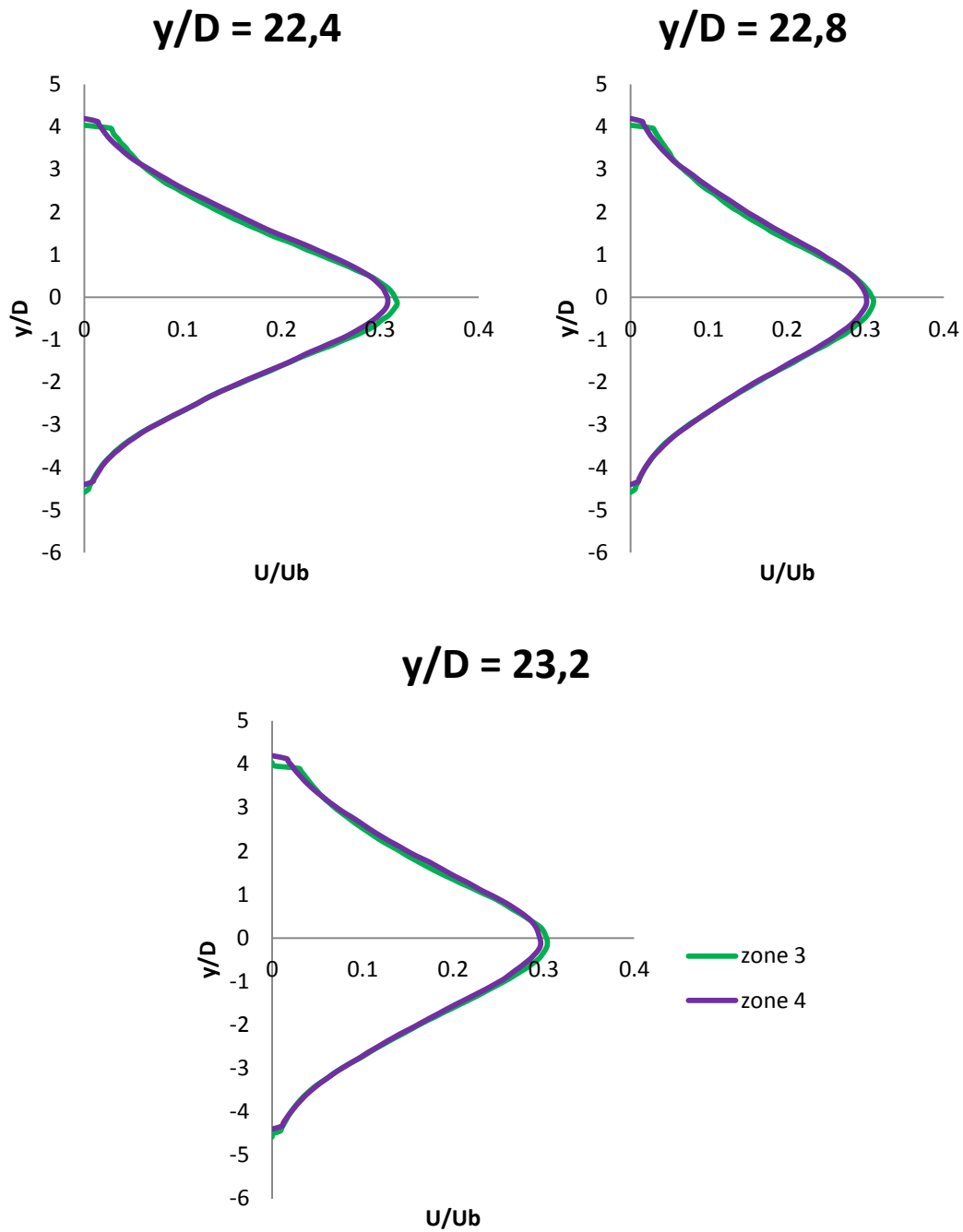


Figure 4.9: Reynolds shear stress profiles in the intersection between zone 2 and 3.

Finally, the intersection profiles for the same magnitudes are showed following in the zone 3 and 4 (see figure 4.10, 4.11 and 4.12).



**Figure 4.10: Streamwise mean velocity profiles in the intersection between zone 3 and 4.**

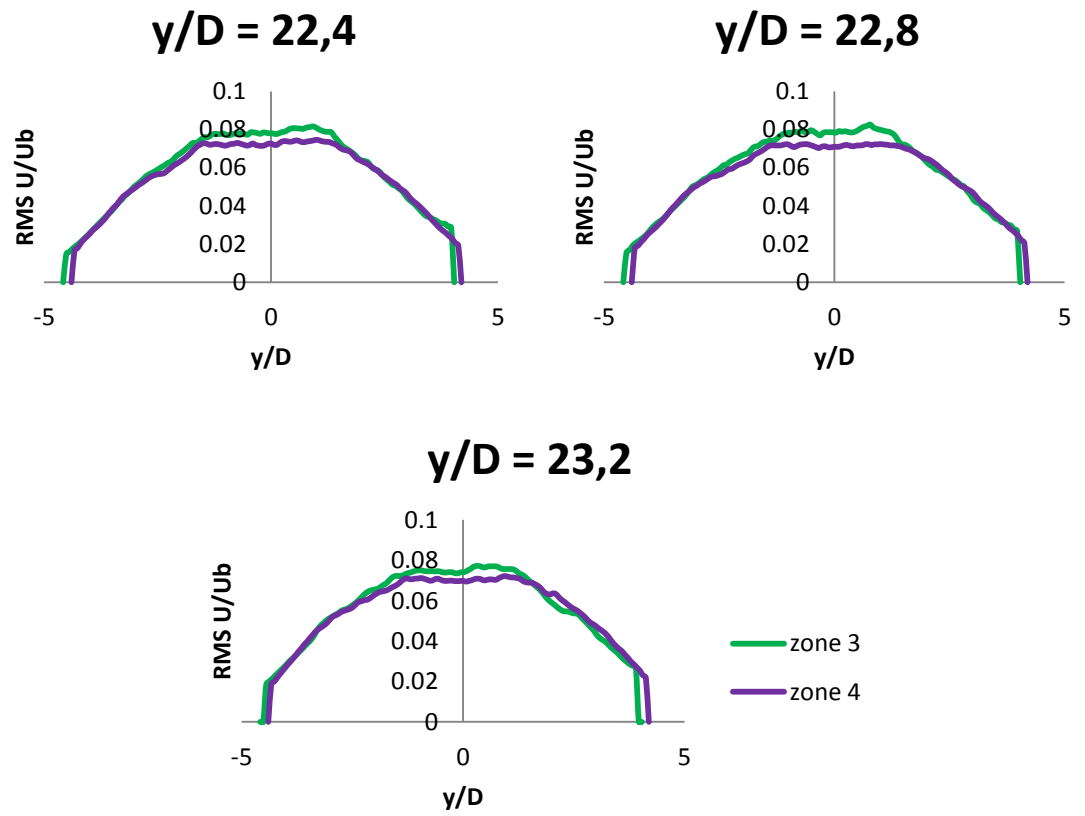


Figure 4.11: Streamwise turbulence intensity profiles in the intersection between zone 3 and 4.

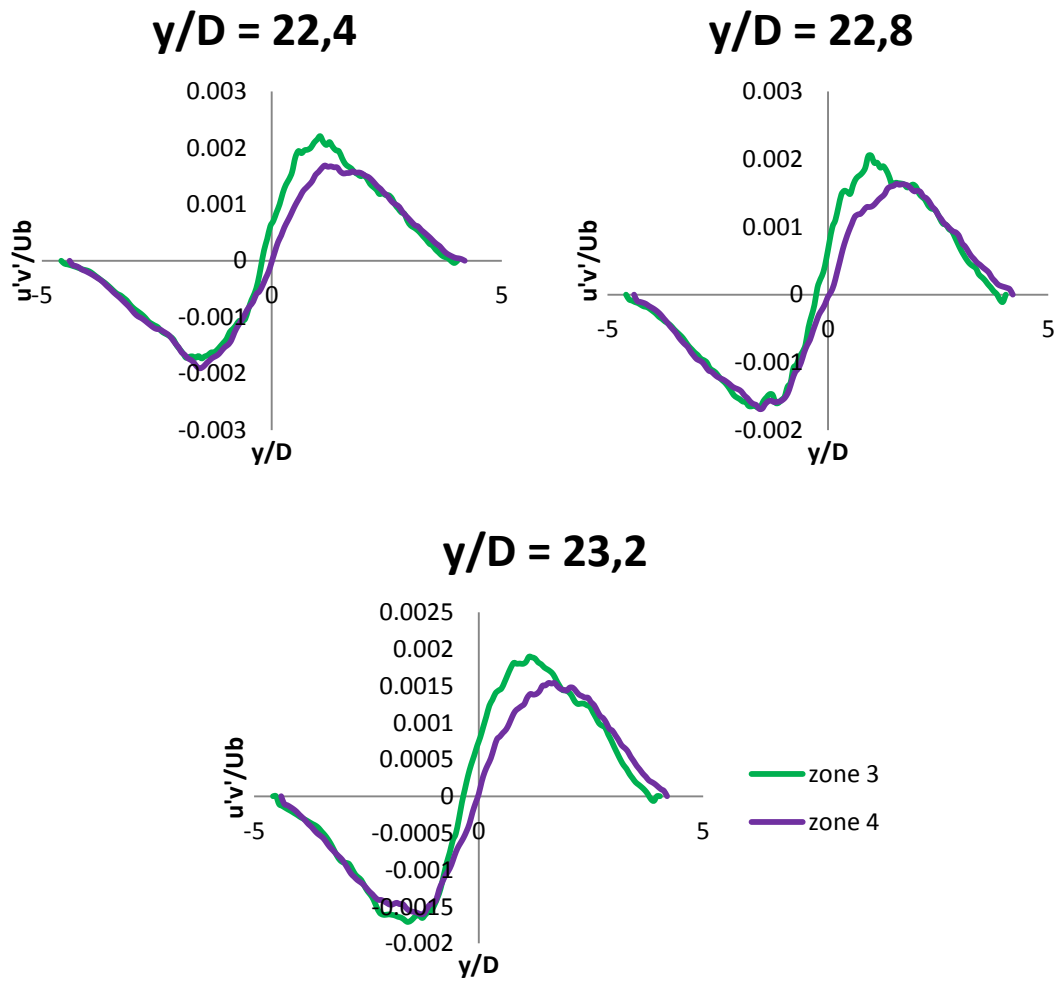


Figure 4.12: Reynolds shear stress profiles in the intersection between zone 3 and 4.

The difference between areas for all the magnitudes and in the different union zones has been solved in the next tables (tables 4.2, 4.3 and 4.4) and the sum of all the area to find the best point of link. The pink square is the minimum area for each magnitude and in the total.

**Table 4.2: Difference area results in the intersection between zone 1 and 2.**

(y/D)1	(y/D)2	(y/D)mean	Vy	RMS Vx	RMS Vy	stress XX	stress YY	Vx	stress XY <sup>2</sup>	Total
7,21	7,19	7,20	20,48	6,37	8,31	0,65	1,08	2,07	0,35	39,31
7,28	7,26	7,27	1,24	1,08	1,71	0,13	0,21	2,04	0,35	6,77
7,34	7,32	7,33	1,13	1,02	1,49	0,13	0,18	2,01	0,35	6,31
7,41	7,39	7,40	1,19	1,02	1,48	0,13	0,17	2,00	0,35	6,35
7,48	7,46	7,47	1,24	1,01	1,45	0,13	0,16	1,98	0,34	6,31
7,55	7,52	7,54	1,27	1,01	1,47	0,13	0,17	1,94	0,34	6,33
7,62	7,59	7,60	1,31	1,03	1,49	0,14	0,18	1,95	0,34	6,42
7,68	7,66	7,67	1,34	1,04	1,48	0,14	0,17	1,96	0,34	6,47
7,75	7,73	7,74	1,36	1,04	1,45	0,13	0,16	1,95	0,33	6,44
7,82	7,79	7,81	1,39	1,02	1,46	0,12	0,17	1,94	0,33	6,42
7,89	7,86	7,87	1,39	1,03	1,47	0,12	0,17	1,92	0,32	6,42
7,96	7,93	7,94	1,42	1,07	1,48	0,13	0,17	1,90	0,33	6,50
8,02	7,99	8,01	1,40	1,14	1,46	0,14	0,16	1,88	0,33	6,49
8,09	8,06	8,08	1,35	1,12	1,42	0,13	0,15	1,85	0,32	6,35
8,16	8,13	8,14	1,35	0,70	1,01	0,04	0,07	1,85	0,30	5,33
8,23	8,19	8,21	0,10	0,85	0,39	0,08	-0,11	1,75	0,27	3,33

**Table 4.3: Difference area results in the intersection between zone 2 and 3.**

(y/D)2	(y/D)3	(y/D)mean	Vy	RMS Vx	RMS Vy	stress XX	stress YY	stress XY	Vx	Total
15,69	15,69	15,69	5,47	0,34	1,79	0,01	0,04	0,32	0,61	8,58
15,63	15,62	15,62	0,09	0,33	0,40	0,01	0,03	0,02	0,55	1,41
15,56	15,55	15,56	0,20	0,56	0,61	0,01	0,06	0,04	0,50	1,99
15,49	15,48	15,49	0,19	0,67	0,67	0,01	0,07	0,05	0,50	2,17
15,43	15,42	15,42	0,18	0,67	0,68	0,01	0,07	0,05	0,52	2,19
15,36	15,35	15,35	0,17	0,65	0,68	0,01	0,07	0,05	0,55	2,19
15,29	15,28	15,29	0,15	0,62	0,68	0,01	0,07	0,05	0,57	2,15
15,22	15,21	15,22	0,14	0,59	0,67	0,01	0,06	0,05	0,56	2,08
15,16	15,14	15,15	0,13	0,58	0,67	0,01	0,06	0,05	0,57	2,06
15,09	15,08	15,08	0,10	0,58	0,68	0,01	0,06	0,05	0,58	2,06
15,02	15,01	15,02	0,07	0,59	0,68	0,02	0,06	0,05	0,56	2,02
14,96	14,94	14,95	0,06	0,58	0,69	0,02	0,06	0,05	0,57	2,02
14,89	14,87	14,88	0,03	0,59	0,69	0,02	0,06	0,05	0,60	2,03
14,82	14,80	14,81	0,03	0,81	0,81	0,02	0,08	0,06	0,65	2,47
14,76	14,74	14,75	0,58	0,76	1,21	0,02	0,07	0,14	0,71	3,49
14,69	14,67	14,68	18,27	6,22	7,86	0,01	0,42	0,67	0,70	34,15

**Table 4.4: Difference area results in the intersection between zone 3 and 4.**

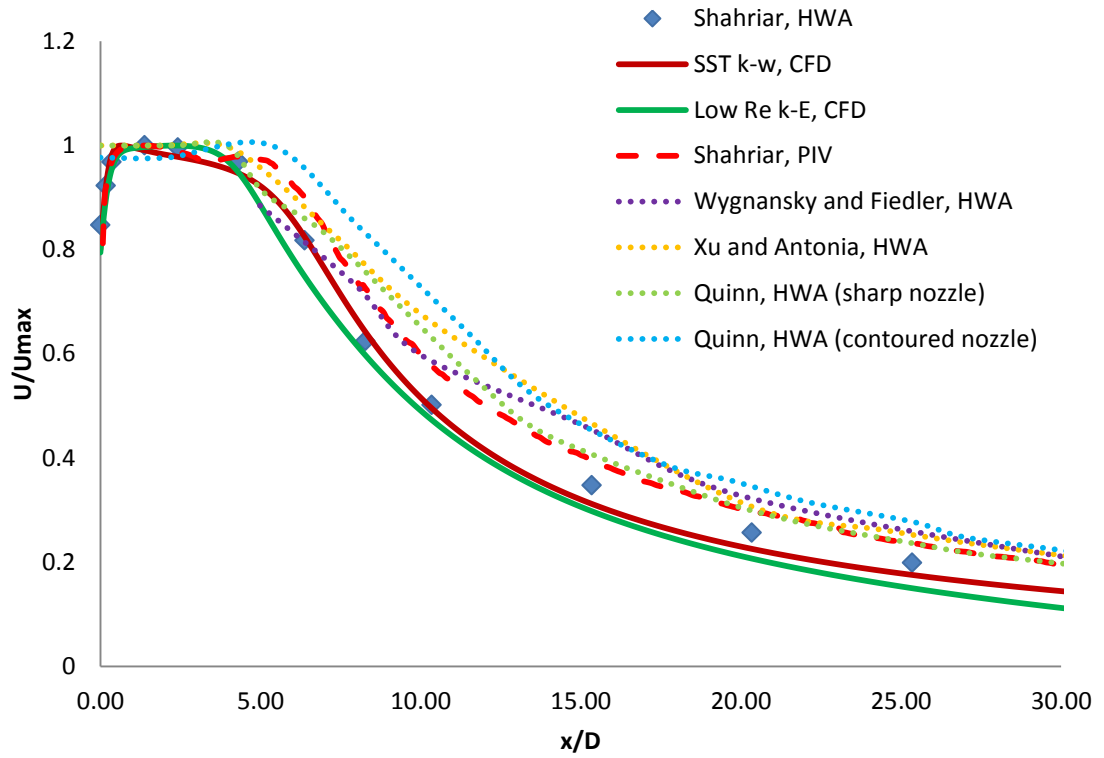
(y/D)3	(y/D)4	(y/D)mean	Vy	RMS Vx	RMS Vy	stress XX	stress YY	stress XY	Vx	Total
23,29	23,30	23,29	18,94	5,83	7,05	0,00	0,28	0,42	0,26	32,80
23,22	23,23	23,23	0,11	0,23	0,08	0,01	0,03	0,02	0,07	0,55
23,15	23,16	23,16	0,02	0,28	0,12	0,01	0,04	0,02	0,05	0,54
23,08	23,10	23,09	0,03	0,56	0,34	0,01	0,07	0,05	0,05	1,12
23,02	23,03	23,02	0,03	0,57	0,35	0,01	0,07	0,05	0,04	1,13
22,95	22,96	22,95	0,04	0,57	0,34	0,01	0,07	0,05	0,05	1,15
22,88	22,89	22,89	0,05	0,56	0,34	0,01	0,07	0,05	0,06	1,14
22,81	22,83	22,82	0,06	0,54	0,32	0,01	0,06	0,05	0,07	1,13
22,74	22,76	22,75	0,08	0,51	0,32	0,01	0,06	0,05	0,08	1,12
22,68	22,69	22,68	0,09	0,49	0,32	0,02	0,06	0,05	0,09	1,11
22,61	22,62	22,62	0,09	0,47	0,33	0,02	0,06	0,05	0,10	1,11
22,54	22,55	22,55	0,09	0,47	0,33	0,02	0,06	0,05	0,11	1,12
22,47	22,49	22,48	0,10	0,48	0,32	0,02	0,06	0,05	0,13	1,15
22,41	22,42	22,41	0,10	0,50	0,31	0,02	0,06	0,05	0,15	1,18
22,34	22,35	22,34	0,08	0,65	0,37	0,02	0,07	0,05	0,13	1,38
22,27	22,28	22,28	0,02	0,68	0,41	0,01	0,07	0,05	0,11	1,37
22,20	22,22	22,21	18,88	6,32	7,43	0,01	0,35	0,49	0,09	33,57

## 4.2 Validation of the PIV data results

The graphics of several magnitudes in comparison with other authors and methods will be showed in this chapter and other important graphics to verify the PIV data.

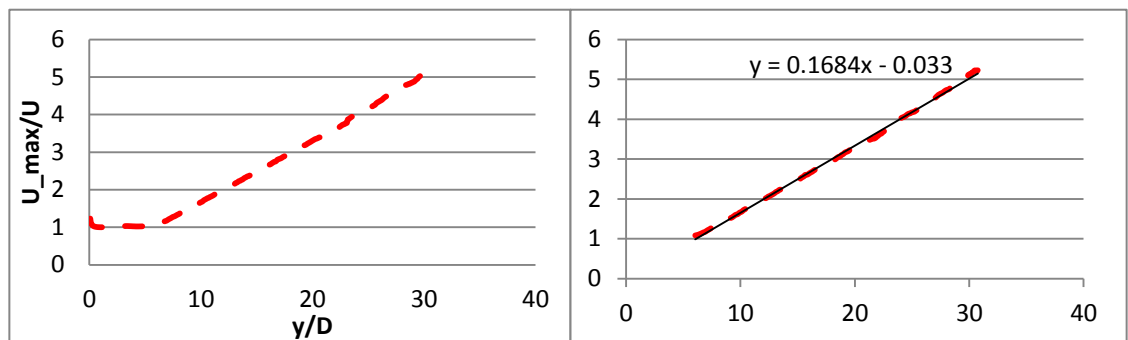
- Streamwise mean velocity decay in the centerline:

In the first picture (see figure 4.13) the streamwise velocity of the PIV method is compared with several authors and methods distinguish with different colors. All data have been divided by maximum velocity of the field.



**Figure 4.13: Streamwise mean velocity decay in the centerline for several authors and methods.**

The inverse function of the same graphic is represented in figure 4.14 and the linear approximation to the slope.



**Figure 4.14: Inverse streamwise means velocity in the centerline for PIV data and the linear function approximation for the slope.**

- Streamwise mean velocity profiles:

In figure 4.10, it is showed the streamwise mean velocity profile in different point of the streamwise axis comparing Hot Wire Anemometer data and Particle Image Velocimetry data for Shahriar measurements, normalized by maximum velocity.

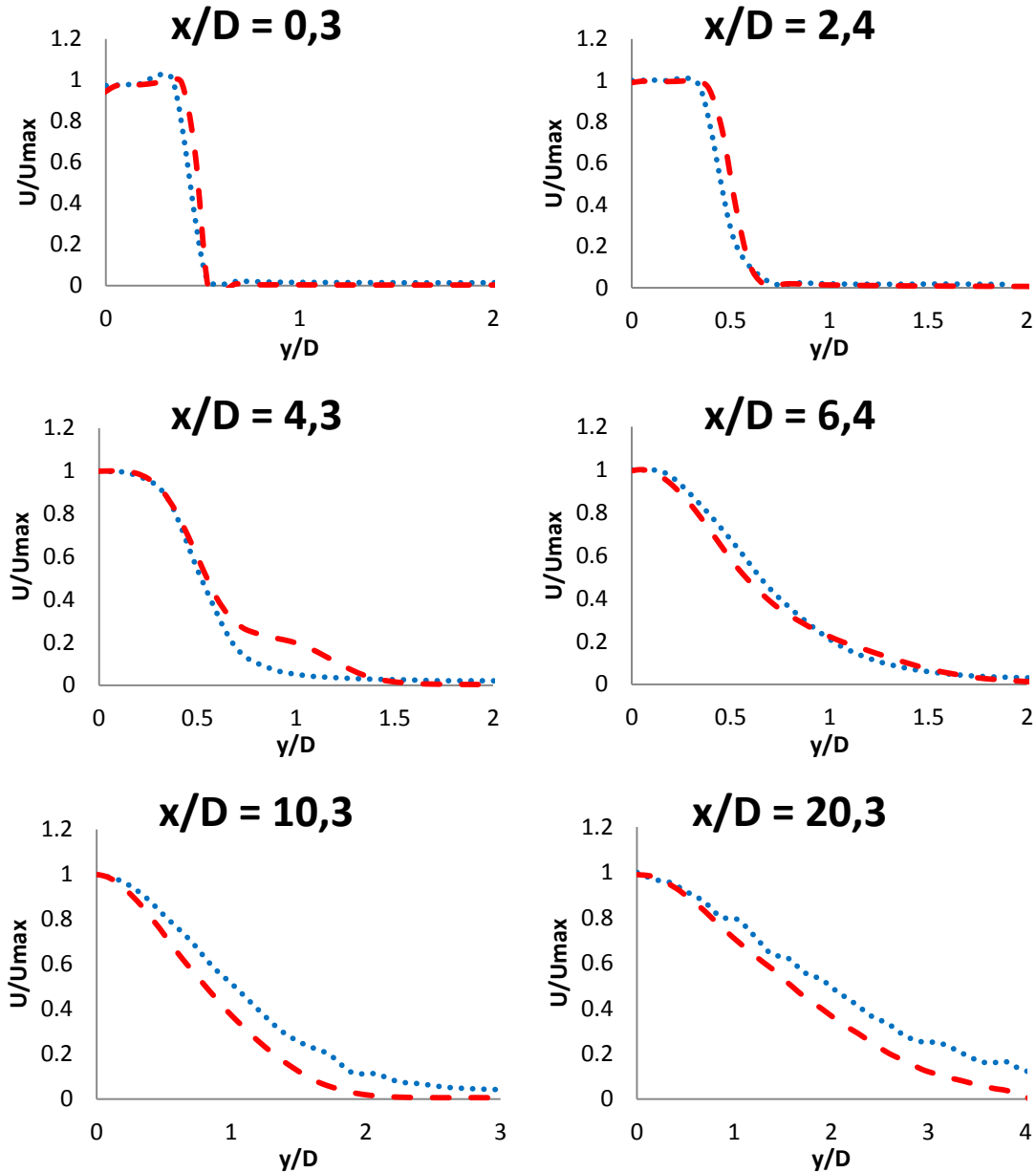
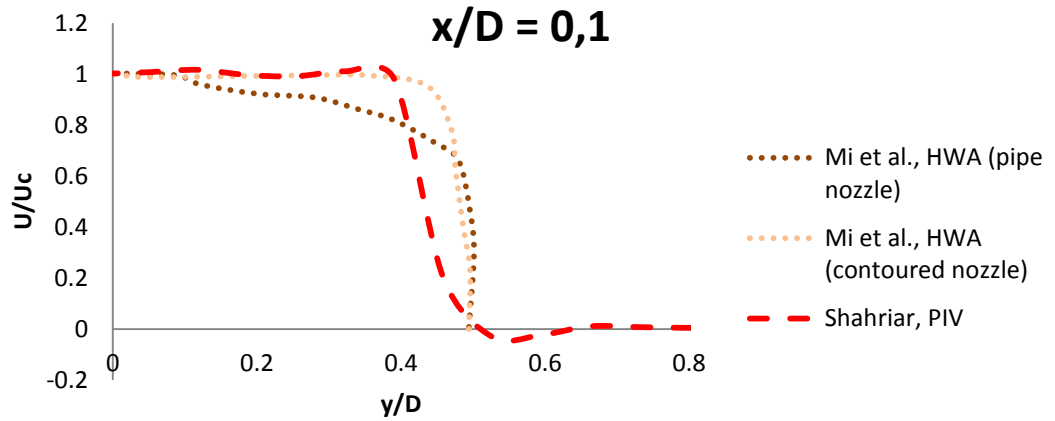


Figure 4.15: Streamwise mean velocity profile in several axial points for HWA method (blue) and PIV method (red) for Shahriar data.

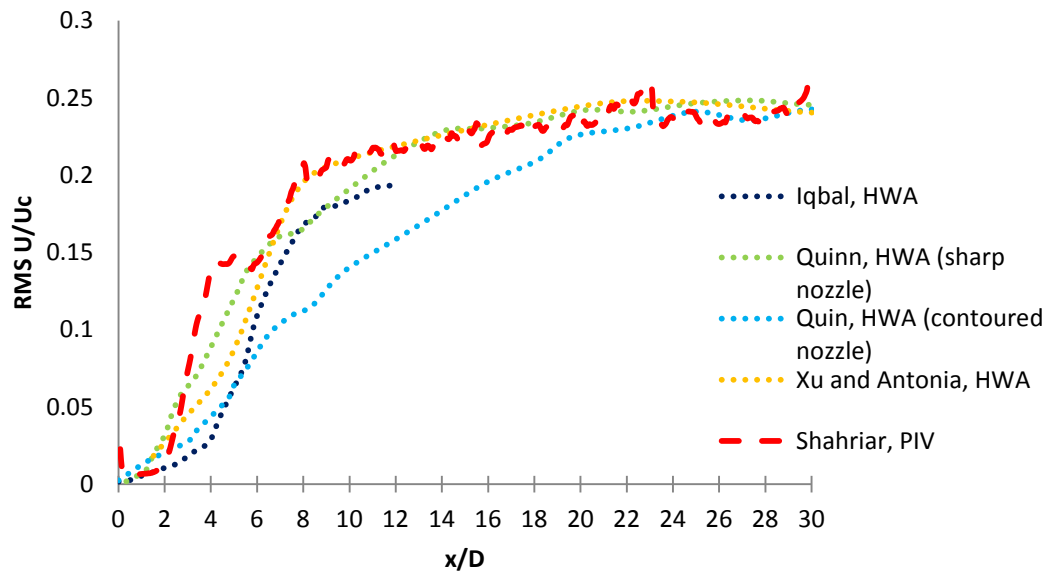
The streamwise mean velocity profile in the near field is represented in figure 4.16, superimposing PIV method and the data of the authors Mi et al. in the same graphic. These data have been standardized by centerline mean velocity.



**Figure 4.16: Streamwise mean velocity profile in the near field for PIV and Mi et al. studies.**

- Centerline streamwise turbulence intensity along the abscissas axis:

Two figures are presented in order represent this magnitude. In the first image (see figure 4.17), the streamwise turbulence intensity has been normalized by the centerline velocity in each point and it is compared with a few old authors results.



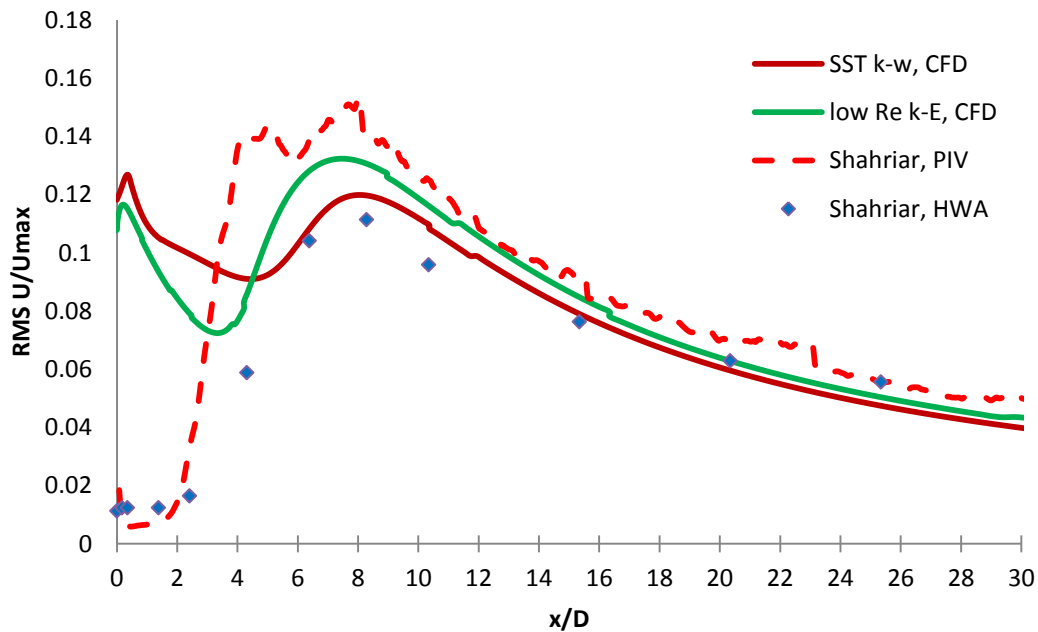
**Figure 4.17: Streamwise turbulence intensity along the centerline normalized by centerline velocity.**

In table 4.5, the principal features of the turbulence intensity have been obtained and compared with other author results.

**Table 4.5: Turbulence plot features for PIV and Todde [17] experiment measures.**

	First peak		Dwell		Second peak		Plateau
	y/D	Level (%)	y/D	Level (%)	y/D	Level (%)	Level (%)
PIV	4,5	14,3	5,4	14,3	8	20,4	24
Todde [17]	4,1	21	6,1	17,5	10	23	23,5

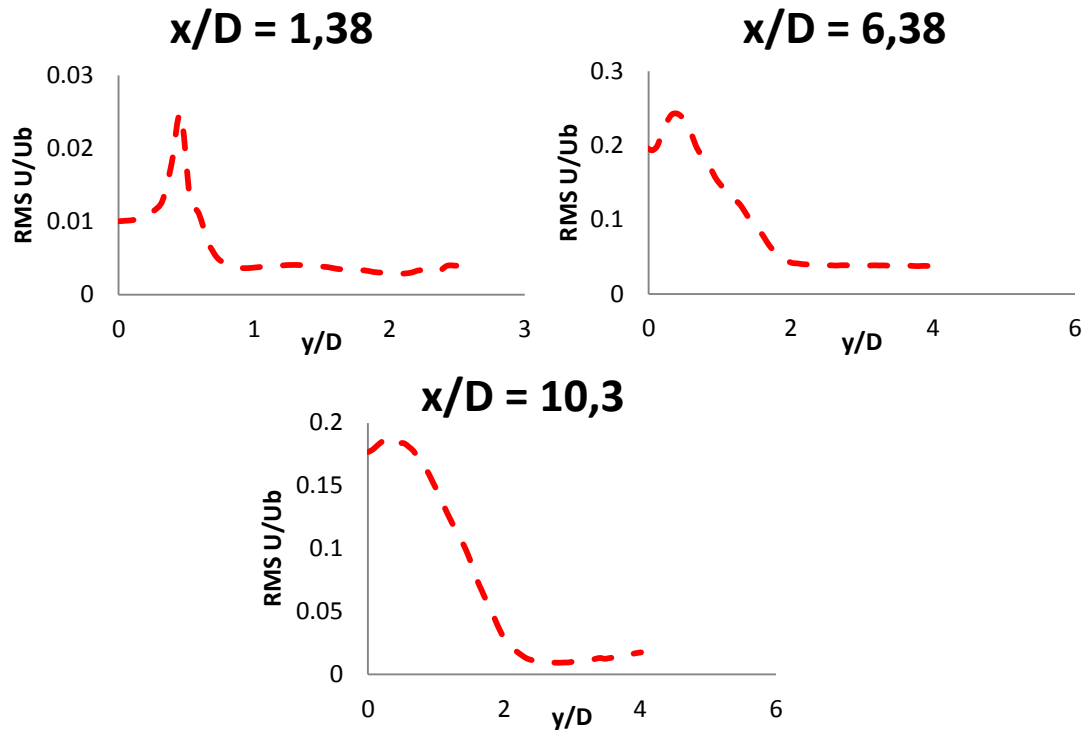
The second graphic (see figure 4.18) shows the same magnitude however, it is normalized by the maximum velocity and it is made a comparison with others data collection methods.



**Figure 4.18: Streamwise turbulence intensity along the centerline normalized by maximum velocity.**

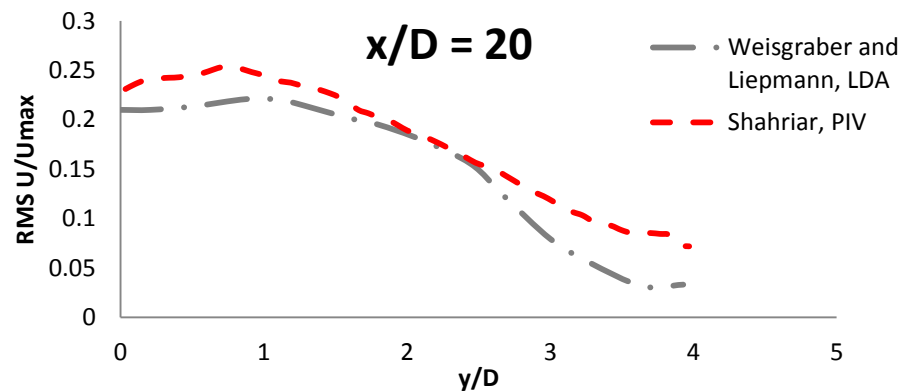
- Streamwise turbulence intensity profiles:

In figure 4.19, turbulence intensity profile is showed in different points in the centerline. PIV method has been used to the data collection and has been normalized by bulk velocity.



**Figure 4.19: Streamwise turbulence intensity profiles in the PIV method.**

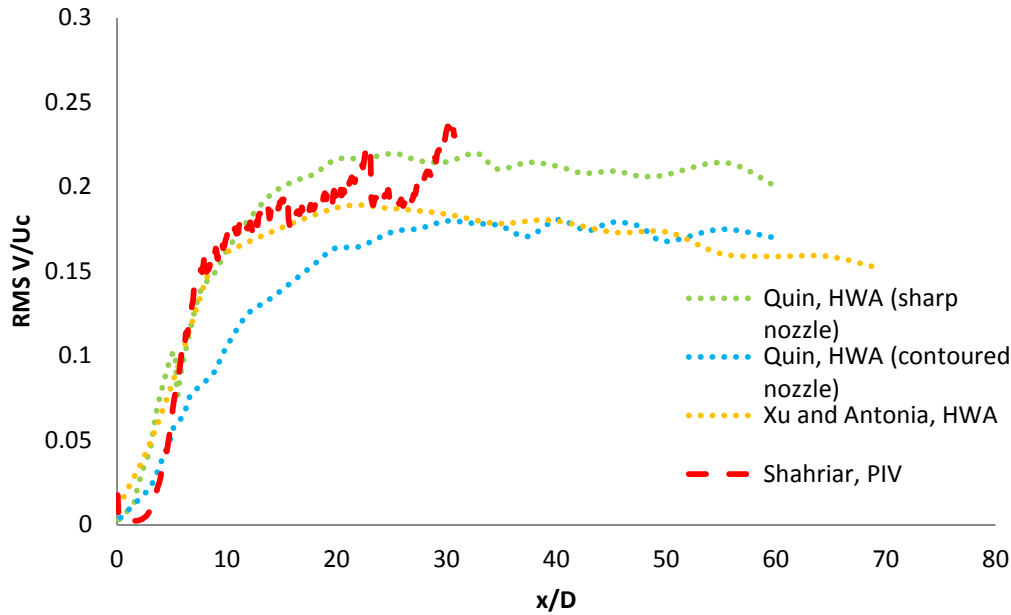
Streamwise turbulence intensity profile in the intermediate field ( $y/D = 20$ ) is presented in figure 4.20 for PIV method and Weisgraber and Liepmann values. The normalization has been provided by maximum mean velocity.



**Figure 4.20: Streamwise turbulence intensity profile in the intermediate field.**

- Radial turbulence intensity along the centerline:

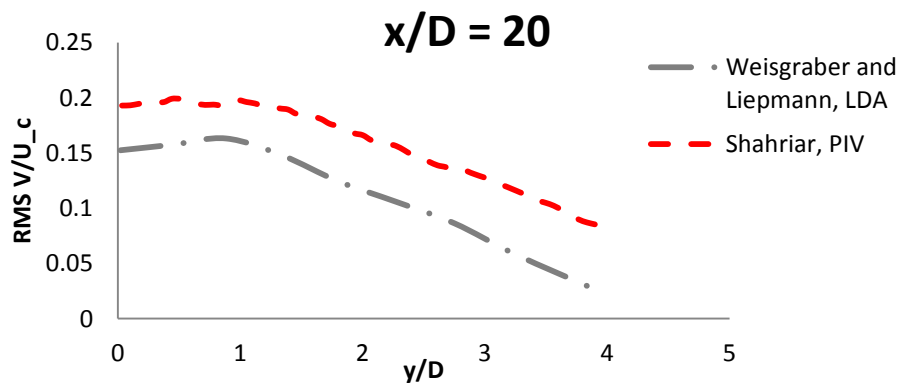
In figure 4.21, radial turbulence intensity is showed along the centerline for PIV data; Xu and Antonia; and Quin, sharp and contoured nozzle has been represented for this author. The data have been standardized by centerline mean velocity.



**Figure 4.21: Radial turbulence intensity along the centerline.**

- Radial turbulence intensity profiles:

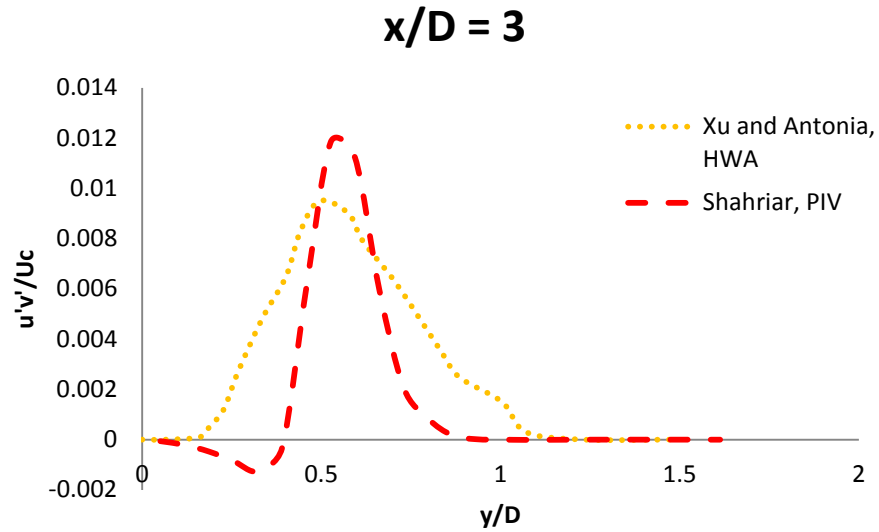
Weisgraber and Liepmann values and PIV method data are compared in figure 4.22 in transition region normalized by centerline velocity in the streamwise direction.



**Figure 4.22: Radial turbulence intensity profile in the intermediate field.**

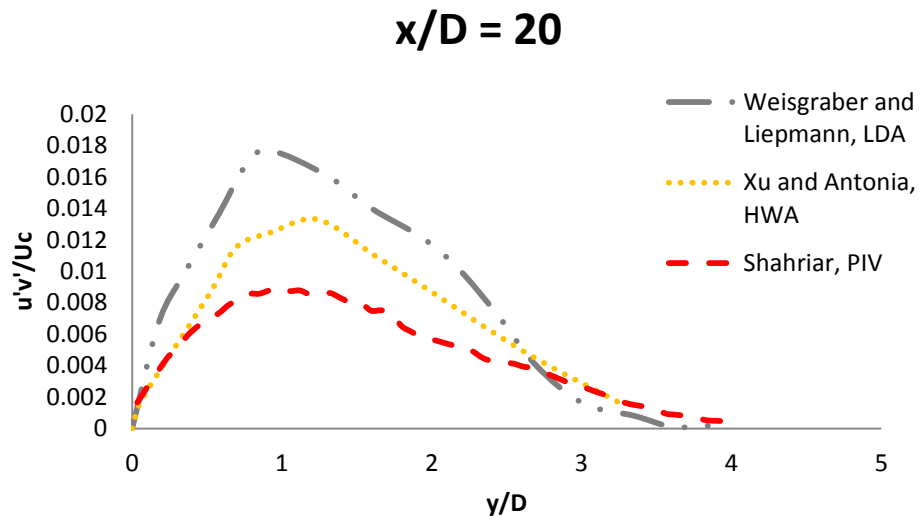
- Reynolds shear stress profiles:

Reynolds shear stress in the near field is presented in figure 4.23 for Xu and Antonia and PIV method data divided by centerline velocity.



**Figure 4.23: Reynolds shear stress profile in the near field.**

Reynolds shear stress profile in transition region for two authors results and PIV method data have been represented in figure 4.24 normalized by the centerline velocity.



**Figure 4.24: Reynolds shear stress profile in the intermediate field.**

- Self-similarity:

Self-similarity streamwise mean velocity normalized by maximum mean velocity for several measurement techniques data, Hot Wire Anemometry (M), SST k- $\omega$  computational method and Particle Image Velocimetry (PIV), are showed in figure 4.25. Moreover, the Gaussian distribution is superposed in the same graphic.

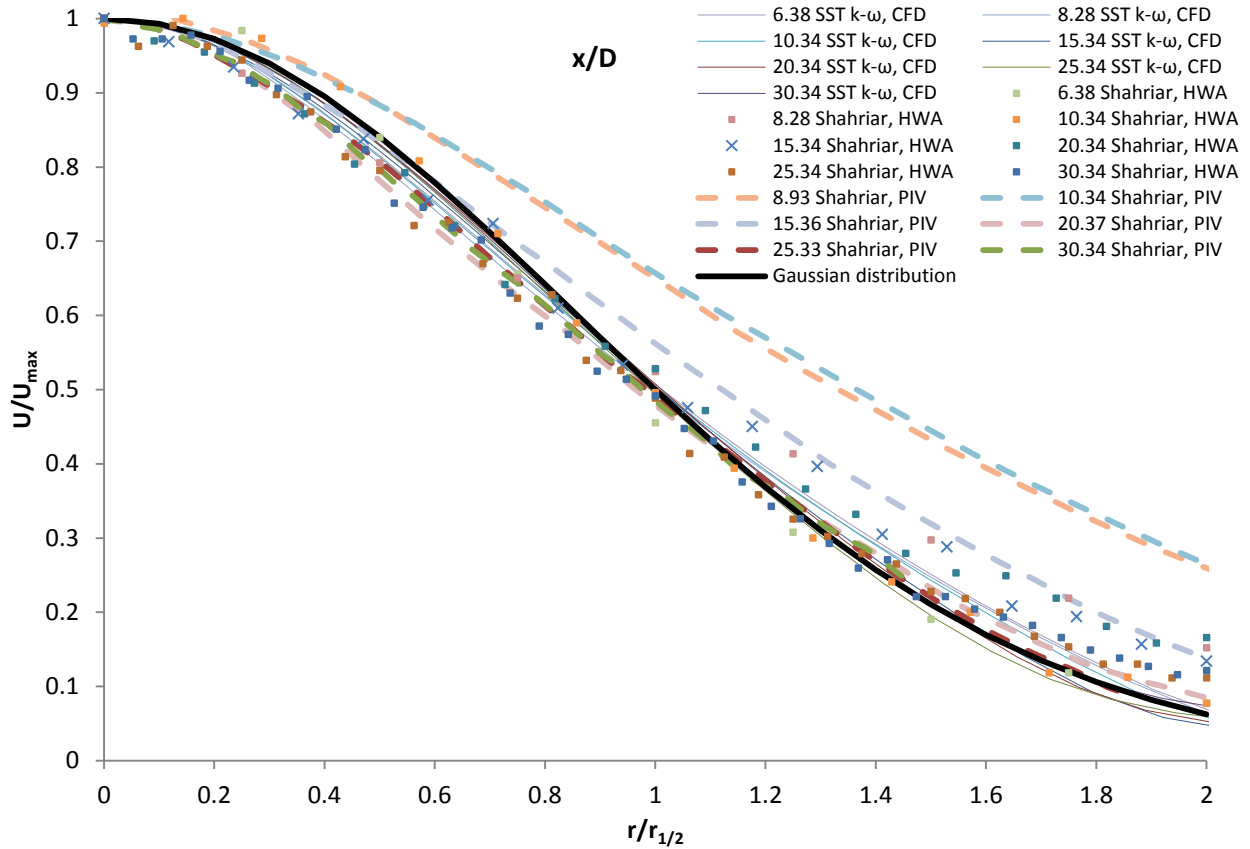
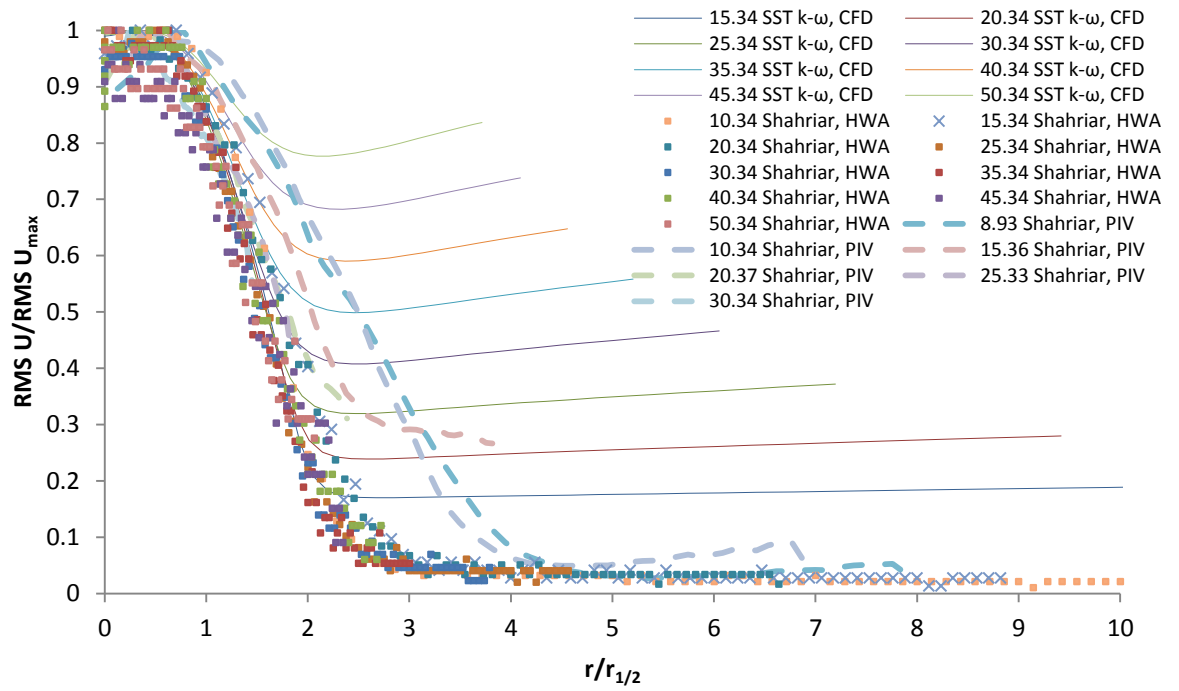


Figure 4.25: Self-similarity streamwise mean velocity for several method data.

Self-similarity streamwise turbulence intensity is presented in figure 4.26 for the same methods that the previous graphic without the Gaussian distribution and normalized by the same magnitude.



**Figure 4.26: Self-similarity streamwise turbulence intensity.**

### 4.3 Results for the analysis in the near and intermediate fields

- Turbulent Kinetic Energy (TKE):

Turbulent kinetic energy decay in the centerline is showed in the next picture (see figure 4.27). The measurements have been obtained with the PIV method.

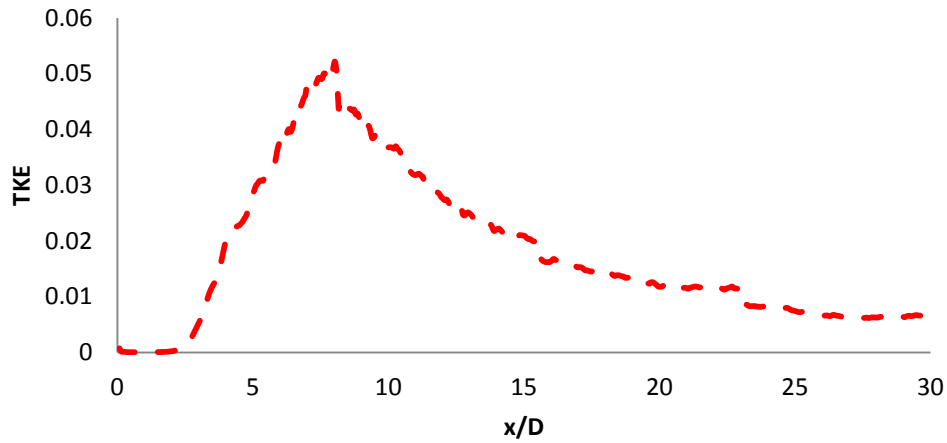


Figure 4.27: Turbulent kinetic energy along the centerline with Shahriar PIV data.

Turbulent kinetic energy in the out of the nozzle is presented in this picture (see figure 4.28):

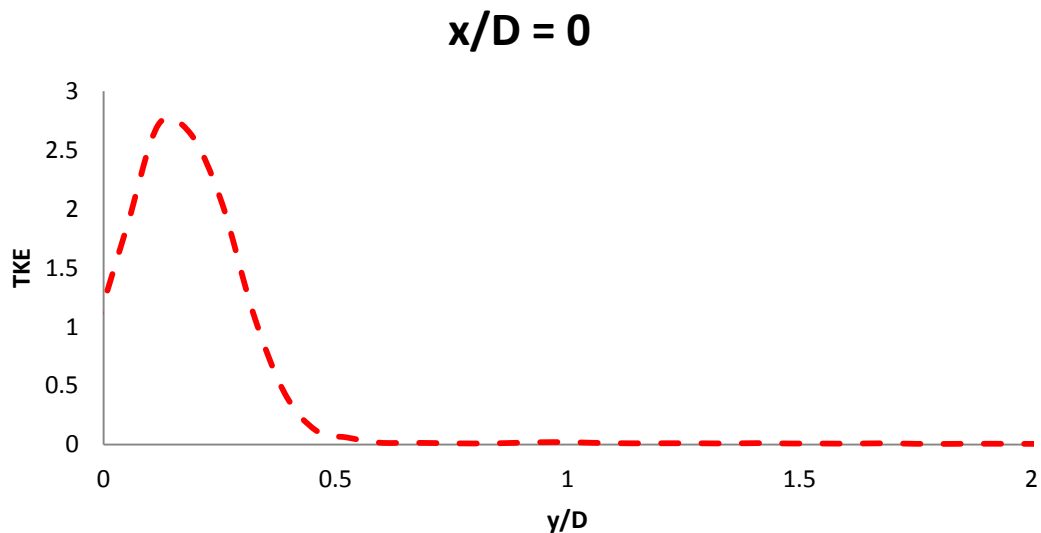


Figure 4.28: Turbulent kinetic profile in the out of the nozzle for Shahriar PIV data.

Turbulent kinetic energy profile obtained of PIV data is presented for four streamwise axial points in the next figure (figure 4.29).

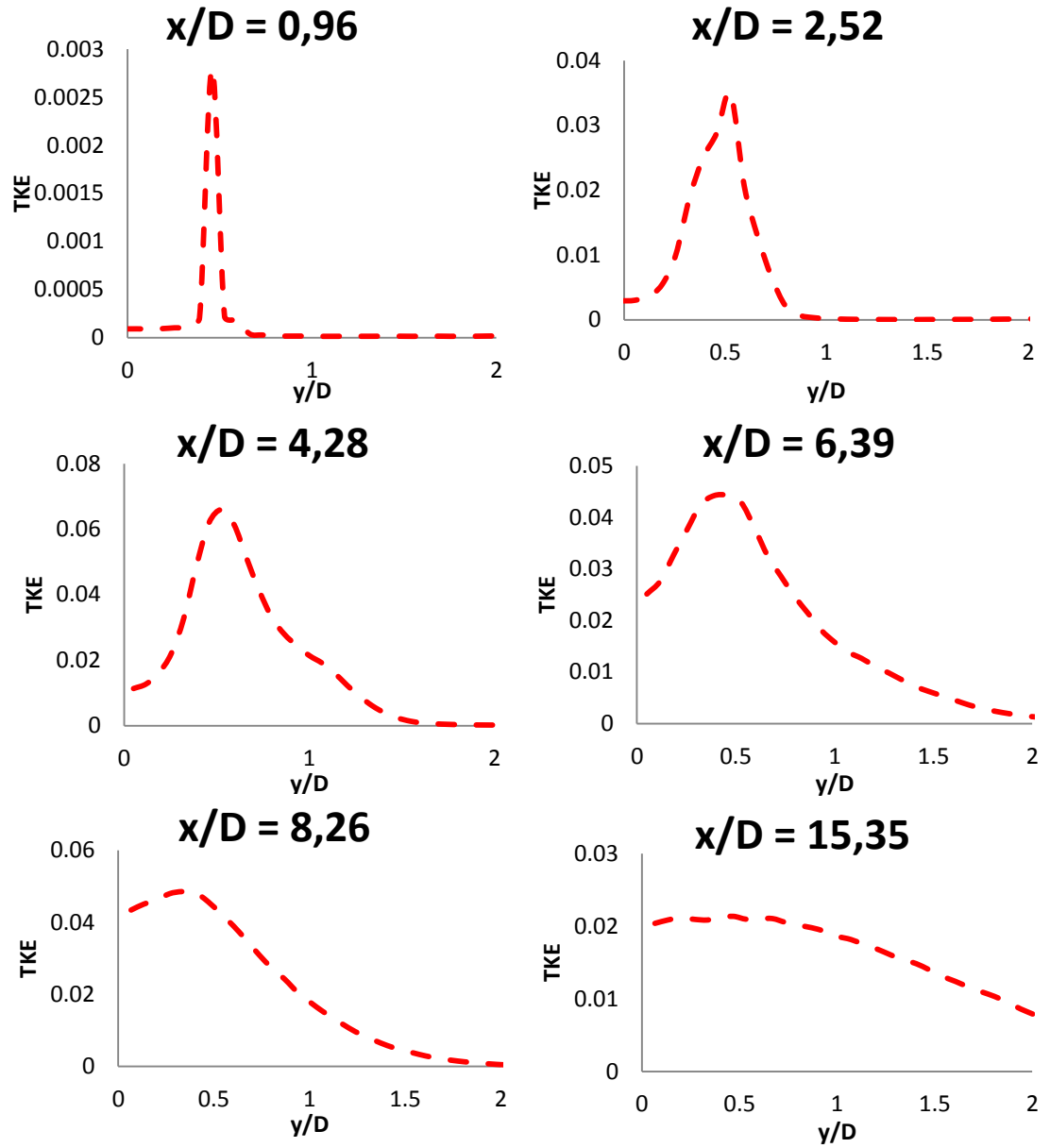
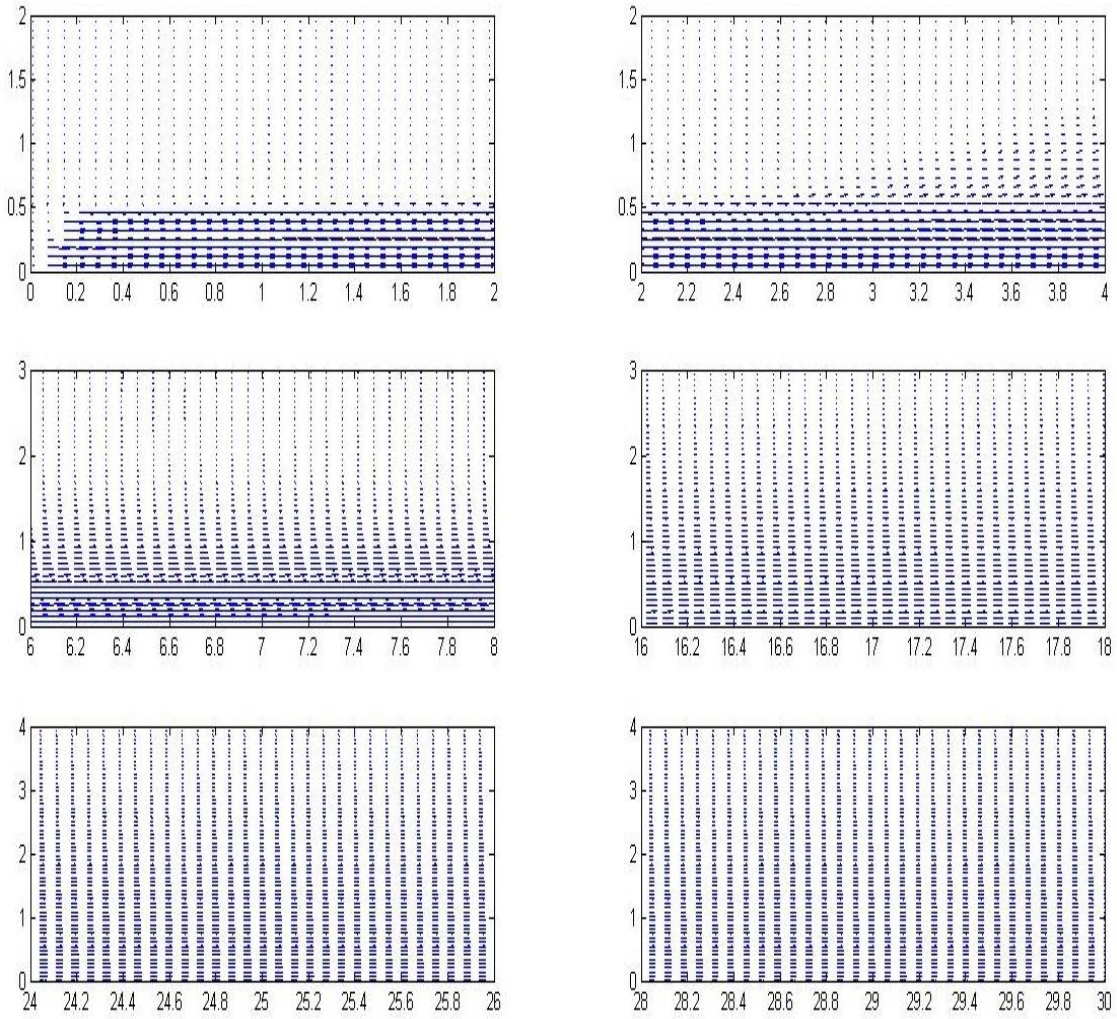


Figure 4.29: Turbulent kinetic energy profile for several points with the PIV method data.

- Vector fields:

They are showed to the mean velocity vectors in figures 4.30.



**Figure 4.30: Velocity field for several regions of the flow represented by vectors.**

## 5 DISCUSSION

In this chapter, the obtained results and the followed method will be analyzed. The followed scheme in the method and the results chapter will be maintained to discuss the results. Moreover, the strengths and the weakness of the project will be presented and commented in order to make a critical view of the thesis.

### 5.1 *Discussion of the processing of the PIV data*

In this section, the objective is the union of the different zones which were created due to the PIV data collection. The first step is the normalization of the PIV data because the distinct zones were measured with different conditions. The bulk velocity has been also calculated in this step. The second step is to find the best points to join the different zones. In order to do it, graphics and area calculations have been obtained.

To calculate the bulk velocity, Reynolds equation and Sutherland's law have been the main principles to obtain it. Applying these rules, the bulk velocity for each zone has been calculated (see table 4.1). These values are about 8,7 m/s for each zones. This is due to the similar test conditions. The conditions analysis of every region has been presented in the same table.

The graphics have been represented for magnitudes decay in the centerline for all the zone at the same time; streamwise mean velocity (fig. 4.1), streamwise turbulence intensity (fig. 4.2) and radial turbulence intensity (fig. 4.3); and for several profiles in the intersection zones with the two functions involved in different points; streamwise velocity (fig. 4.4, 4.7 and 4.10), streamwise turbulence intensity (fig. 4.5, 4.8 and 4.11) and Reynolds shear stress (fig. 4.6, 4.9 and 4.12). Others magnitudes were represented and evaluated also in the project but they are not included in the report because they do not improve the results.

These differences among the same magnitude in the same point obtained with two different camera positions are due to the time to obtain the mean magnitude at 1 Hz is short. Then, mean magnitudes can varying between two different camera positions.

It has been difficult to find the best point to link every zone with this qualitative method due to the similarity between the functions of the zones in the same graphic and the similarity in the different points of the axis of abscissas. It is good because

the data in the adjacent zones are really similar and the data collection method very accurate. Then, it has been necessary to use other method.

Different areas have been calculated to solve the previous problem of similarity. The solutions for all the magnitudes and points in the intersection zone have been presented in table 4.2, 4.3 and 4.4. In each table have been solved one intersection and the minimum value have been stood out with pink color both the letter and the box. The total different areas have been calculated, thus, the best intersection point have been the minimum value of these column. Then, the link point has been concluded as this one.

## **5.2 Discussion about the validity of the PIV data**

In this section, it will be validated the PIV data in comparison with old author studies and other measurement methods.

- Streamwise mean velocity decay in the centerline:

The potential core ( $y/D < 5$ ) is approximately constant how it is possible to see in figure 4.13, but a slight oscillation is produced in the PIV function due to the flow itself. The amplitude of this oscillation is depended of the Reynolds number. Others little divergences are due to the Reynolds number and the geometry of the contraction nozzle. In conclusion, the potential core value of the PIV data is normal and similar to the other authors and measurement techniques [17].

In the transition zone, the streamwise velocity decrease until the flow stops along the abscissas axis. The behavior of this magnitude for the PIV measurement is similar of the old authors and measurement techniques (see figure 4.13). In this zone, the inverse function has been represented (see figure 4.14). The slope and the initial point in the abscissas axis have been obtained. PIV Reynolds number is 3290, then the slope of PIV data (0,168) is smaller than the Todde data (0,215) for similar Reynolds number (see table 2.1). It is due to the nozzle geometry and the wall position in relation to the nozzle that are not the same. This region PIV values are coherent in comparison with other authors and methods.

- Streamwise mean velocity profiles:

In figure 4.15, it can be seen that the PIV and HWA results are equal with few discrepancies in the final points ( $y/D > 10$ ). It is appreciated also the evolution of the velocity profile along the centerline. In the first, the profile takes saddle-back shape ( $y/D = 0,3$ ); following ( $y/D=2,4$ ), it take top-hat shape; and finally it evolves in a Gaussian shape ( $y/D > 4,3$ ) [19].

In figure 4.16, Mi et al. profile in the early zone has been compared for contraction and pipe nozzle. Pipe profile is round, while contraction nozzle take saddle-back shape. PIV measurement is similar to the contraction nozzle function due to PIV nozzle is contracted. The maximum value of the velocity normalized is 1,08, it is similar to other studies [18]. It is due to the vena contract effect causing an initial narrowing of the jet cross section.

- Centerline streamwise turbulence intensity profile:

In figure 4.17 is showed this magnitude normalized by centerline mean velocity. In the first region ( $1 < y/D < 5$ ), the turbulence intensity increases until the first local peak, it is placed in  $y/D \approx 5$ , depending of Reynolds number. The next zone ( $5 < y/D < 7$ ), this magnitude decreases and in  $y/D \approx 7$  is found the local minimum. Farer in the axis ( $7 < y/D < 10$ ), turbulence intensity increases where is found the global maximum in  $y/D \approx 10$ . Finally, it is established adiabatically.

The similarity between PIV and other authors function have not followed the same pattern, but in the next table (table 4.5), the verification of the PIV data is showed in comparison with Todde study [17]. The differences between them are caused for the difference in the nozzle geometry and the length between the nozzle out and the wall.

Figure 4.18 represents the turbulence intensity normalized by the maximum velocity. The turbulence intensity value is higher in the PIV data because the Reynolds number (3290) is lower than CFD and HWA number (3461). The near zone turbulence intensity is not represented correctly by the CFD techniques due that the near zone laws are not accuracy. The route followed by the different measurement methods is similar.

- Streamwise turbulence intensity profiles:

In other studies [3], a peak is observed in the early field ( $y/D = 1$ ) in a radial distance  $0,5 \cdot D$  and with an absolute value of 0,025; similar to PIV data where in the same point the peak is appeared in  $0,46 \cdot D$  and with the same value (see figure 4.19). In the next point ( $y/D = 6$ ), the down slope is longer.

In the next figure (see figure 4.20), this magnitude has been compared with Weisgraber and Liepmann profile and the evolution of the function is equal in the transition region ( $y/D = 20$ ).

- Radial turbulence intensity decay in the centerline:

This magnitude is compared with old author studies in figure 4.21. The similarity between all of them and PIV functions is higher with the radial turbulence intensity normalized by centerline streamwise mean velocity. It can be seen in the early zone, radial turbulence intensity is null ( $0 < y/D < 2$ ). Following, there is a strong slope increase until  $y/D = 8$  which reaches a value of 0,15. Finally, the turbulence intensity is established in 0,2 value.

- Radial turbulence intensity profiles:

Weisgraber and Liepmann study and PIV data have been compared in figure 4.22 where the evolutions of the radial turbulence intensity in the radial direction are similar but PIV value is higher than the function of the author in all the points. It is due to the difference Reynolds number and nozzle geometry.

- Reynolds shear stress profiles:

The Reynolds shear stress profile have been represented to the same time between PIV values and old author's data in the near field (figure 4.23) and transition region (figure 4.24). In the early region, the PIV function is slightly slimmer and higher than Xu and Antonia profile. In the intermediate field, PIV data has followed the pattern that old authors but it has been smaller than Weisgraber and Liepmann and Xu and Antonia profiles. It is due to the nozzle geometry that it is not the same.

- Self-similarity:

Self-similarity streamwise mean velocity have been related with other measured methods in figure 4.25. The self-similarity for PIV method starts in  $15 \cdot D$  approximately and for others methods it happens in  $6,38 \cdot D$ . Although in PIV self-similarity,  $8,28 \cdot D$  points is like the Gaussian distribution.

Self-similarity streamwise turbulence intensity has been showed in figure 4.26. This magnitude follows a pattern and the PIV data is similar to the rest of the techniques in the different streamwise axis points.

### **5.3 Discussion of the results for the analysis**

In this chapter, others magnitudes and plots results that have not been used to verify the PIV data will be explained to complete the analysis of the near field in addition to the magnitudes results explained before that have already been commented.

- Turbulent kinetic energy:

In figure 4.27, TKE decay in the centerline has been represented. In the early region ( $0 < y/D < 2$ ), it is null due to the turbulence intensities are null also and here the flux is expanded in the axial direction and not in the radial. In the next zone (until  $y/D = 8$ ), TKE energy has increased until it has reached the maximum point of the function. After, the function has decreased gradually tending to zero.

In figure 4.28, the turbulent kinetic energy is exposed in the near field. An high point for this magnitude is found in this part of the flow, then a eddy would be formed in the out of the nozzle.

Figure 4.29 shows that the turbulent kinetic energy increases the maximum value until point  $y/D = 4,3$ , also the area of the magnitude develops radially but the maximum value decreases along the centerline later that the maximum point obtained.

It can be seen that the biggest eddies will create in the zone between near and intermediate region, due to the combination between maximum value and area are here. In the early zone, eddies can be formed in the intersection between flow and outside fluid

(shear layer). In the intermediate region, the TKE leaks energy and increases the area where is potentially active. Then, eddies will be generated but the dimensions will be small.

- Vector fields:

Figure 4.30 shows the evolution of the velocity field in the streamwise axis. In the grown zone, the velocity is expanded in the flow direction until  $y/D = 3$ . Once that this point is passed, it can be seen in the figure that the flow is beginning to expand in the radial direction and the stream is slower. It occurs until the final of the transition zone where the flow is slow and expanded in all the volume. In this point, the flow is established and the far field starts.

- Self-similarity:

Figure 4.25 shows that self-similarity streamwise mean velocity follows the Gaussian distribution in the intermediate field and for a low Reynolds number. The results indicate that the CFD method (SST k- $\omega$ ) is accuracy in the transition zone for this magnitude. The near field does not follow the Gaussian distribution, then, the near field is not defined by this magnitude. In order to analyze PIV measurements, the Gaussian distribution pattern later than for the other methods. It is due to some half radius points in the early region are not very accuracy. Maybe for the method employed to obtain them.

Self-similarity streamwise turbulence intensity follows the same pattern in the measurement methods (see figure 4.26). The CFD method does not take the same trajectory. In this method, the profiles near to the nozzle follow better the pattern than far contours.

Transition zone can be defined by self-similarity graphics. For the CFD programs, it is possible to predict this magnitude for the mean velocity, but no very well for the turbulence intensity.

- Streamwise mean velocity:

Inverse streamwise mean velocity decay in the centerline in the transition zone is a lineal function that starts approximately in  $y/D = 7$  (it depends of Reynolds number) and has a slope that depends on the Reynolds number, the geometry of the nozzle and nozzle length to the wall (see figure 4.14). Then, this magnitude is possible to predict by the next equation:

$$\frac{U}{U_{max}} = k \cdot \frac{D}{X - X_p}$$

Where  $k$  is the velocity decay coefficient,  $D$  is the diameter of the nozzle and  $X_p$  is the virtual origin (see table 2.1).

Profiles for this magnitude have the same evolution for all the flows (see figure 4.15). Firstly, saddle-back shape is formed in the grown region with the maximum value of the velocity. It is due to the vena contracted effect. Secondly, top-hat shape develops in the middle of the near zone that is evolved in a Gaussian shape along the near and transition zone. The maximum mean velocity decreases along the centerline.

#### **5.4 Strengths and weakness of the work**

The processing data method, results and discussion have been strength in the work because both the normalization of the data and the link of every zones have been studied in depth. The parameter to normalize the data, bulk velocity, have been obtained with the correct method and for the link of all the regions two different methods have been used to find the best point. Several figures and tables have been showed to corroborate the discussion.

Validation of the PIV data method has been simple, but it has been effective and enough. The results for all the magnitudes have been depending of the external information available. In general, the data have been enough but for some of the magnitudes, radial turbulence intensity and Reynolds shear stress, the information has been limited. Others works have provided a lot of useful information.

Analysis of the near and intermediate region of the flow has been the weakness of the work, due to it is the most difficult part of the investigation but some interesting results have been obtained and discussed.



## 6 CONCLUSION

The principal objectives of this work have been divided in three parts; processing of the PIV data, validity of the PIV data and analysis of the near and intermediate region of the flow. In the first part, the normalization and joining the data have been carried out, in the second one, the comparison with other authors and methods has checked the PIV values, and finally, the analysis has contributed to know better this region of the flow and to verify other studies assumptions.

In the first section, the bulk velocity has been calculated and showed in table 4.1 to normalize all the data of the different zones of measurement and to can linking the different regions. This physical quantity has been around 8,7 m/s depending of the analysis condition in each zone.

Once these actions were done, the best points to join the different zones have been looked for. Firstly, a qualitative method has been used. In order to do it, many graphics have been showed, but the similarity from the data of the different regions in the intersections zones has been impossible to find the best point. Then, a quantitative method has been employed. The difference areas for all the possible magnitudes and points have been showed in table 4.2, 4.3 and 4.4. In order to do it, an accuracy link points have been found.

In the second section, every magnitude have been compared and commented with old authors and other methods of data collection or with other report results. The similarity between all of them has allowed saying that the PIV data have been correct and the data can be analyzed. The principal differences have been caused by different Reynolds number, nozzle geometry and nozzle length to the wall.

These two parts can be checked and improved if in data collection camera positions and frequencies are used. Then, several data in a same flow would be compared and the best of them would can choice. Moreover, time used to data collection can be increased to improve the similarity among the different magnitudes in the same axial point for two camera positions.

The last part of the thesis, an analysis of the near and intermediate field of the flow has been made. The turbulent kinetic analysis and turbulence intensity field have

showed that the eddy formation is more probably in the intersection between the near and transition region ( $3 < y/D < 11$ ) because the momentum is maintenance and mass flow rate increased. Also, in the out of the nozzle, a vortex can be formed due to the intersection between the flow and the outdoor fluid.

Moreover, it has been obtained an equal behavior between the self-similarity streamwise mean velocity and the Gaussian distribution in the intermediate field for all the profiles and a pattern have been found for the self-similarity turbulence intensity in the near field.

Finally, in the transition region, a lineal equation dependency has been confirmed for the inverse streamwise velocity decay. In this equation, the terms have been demonstrated that depend of the Reynolds number and nozzle geometry.

This part can be continued and improved. Other Reynolds number can be analyzed and compared with the actual results to check the evolution of the flow and to obtain similarities them.

## REFERENCES

- [1] Wikipedia. Available at website: [www.wikipedia.org](http://www.wikipedia.org). Accessed 22<sup>th</sup> May.
- [2] Adel Abdel-Rahman. A Review of Effects of Initial and Boundary Conditions on Turbulent Jets. Department of Mechanical Engineering, Beirut Arab University (BAU), Beirut, P.O.B: 11-5020, 2010
- [3] C.G. Ball, H. Fellouah, A. Pollard. The flow field in turbulent round free jets. *Progress in Aerospace Sciences* 50 1–26, 2012.
- [4] Karsten Staack, Reinhard Geisler, Andreas Schröder, Dirk Michaelis. 3D3C-coherent structure measurements in a free turbulent jet. 15th Int Symp on Applications of Laser Techniques to Fluid Mechanics, Lisbon, Portugal. July 2010.
- [5 ] Christopher G. Ball and Andrew Pollard. A Review of Experimental and Computational Studies of Flow from the Round Jet. Computational and Experimental Fluid Dynamics Laboratory Department of Mechanical and Materials Engineering, Queen's University Kingston, Ontario, Canada, internal report no. CEFDL/2007/01. June 2007.
- [6] Siavash Narimousa, Robert R. Long and Serge A. Kitaigorodski. Entrainment due to turbulent shear flow at the interface of a stably stratified fluid. Department of Earth and Planetary Sciences, The Johns Hopkins University, Baltimore, Maryland 21218, 1985.
- [7] Luca Facciolo and Nils Tillmark, Alessandro Talamelli, P. Henrik Alfredsson. A study of swirling turbulent pipe and jet flows. *Physics of fluids* 19, 035105, 2007.
- [8] Vouros, Th. Panidis. Turbulent properties of a low Reynolds number, axisymmetric, pipe jet. *Experimental Thermal and Fluid Science* 44 (2013) 42–50, 2013.
- [9]Kevin Daniel Galli. Hot-Wires Measurements of Statical and Spectral Evolution of an Axisymmetric Turbulent Jet. Massachusetts institute of technology, 1991.
- [10] Efunda. Available at website: [http://www.efunda.com/designstandards/sensors/hot\\_wires/hot\\_wires\\_theory.cfm](http://www.efunda.com/designstandards/sensors/hot_wires/hot_wires_theory.cfm). Accessed 4<sup>th</sup> June.
- [11] R. J. Adrian. Twenty years of image particle velocimetry. *Experiments in Fluids* 39: 159–169, 2005.
- [12] Ye Cheng. A study of the fine-scale three-dimensional flow structures in turbulence using time-resolved stereoscopic scanning particle image velocimetry. The State University of New Jersey, 2011.
- [13] S. V. Alekseenko, A. V. Bilsky, and D. M. Markovich. Application of the Method of Particle Image Velocimetry for Analyzing Turbulent Flows with a Periodic Component. *Instruments and Experimental Techniques*, Vol. 47, No. 5, 2004, pp. 703–710, 2004.

- [14] C. Fukushima, L. Aanen, J. Westerweel. Investigation of the Mixing Process in an Axisymmetric Turbulent Jet Using PIV and LIF. Laboratory for Aero and Hydrodynamics Delft University of Technology Rotterdamseweg 145, 2628 AL Delft, The Netherlands.
- [15] W. Sutherland. The viscosity of gases and molecular force. Philosophical Magazine, S. 5, 36, pp. 507-531, 1893.
- [16] Shahriar Ghahremanian and Bahram Moshfegh. Evaluation of RANS Models in Predicting Low Reynolds, Free, Turbulent Round Jet. Journal of Fluids Engineering Vol. 136 / 011201-1, 2013.
- [17] Valentino Todde, Pier Giorgio Spazzini, Mats Sandberg. Experimental analysis of low-Reynolds number free jets. Exp Fluids 47:279–294, 2009.
- [18] J. Mi, D. S. Nobes and G. J. Nathan. Influence of jet exit conditions on the passive scalar field of an axisymmetric free jet. J. Fluid Mech., vol. 432, pp. 91–125, 2000.
- [19] Shahriar Ghahremanian, Klas Svensson, Mark J. Tummers, Bahram Moshfegh. Near-field mixing of jets issuing from an array of round nozzles. International Journal of Heat and Fluid Flow 47 84–100, 2014.
- [20] Kareem Akhtar. Numerical Investigation using RANS Equations of Two-dimensional Turbulent Jets and Bubbly Mixing Layers. Master of Science in Engineering Science and Mechanics, Virginia, 2010.
- [21] Elizabeth Smith, Jianchun Mi, Graham Nathan and Bassam Dally. The "Round Jet Inflow-Condition Anomaly" for the  $k-\epsilon$  Turbulence Model. School of Mechanical Engineering, University of Adelaide (Australia).
- [22] D. Kuzmin and O. Mierk. On the implementation of the  $k-\epsilon$  turbulence model in incompressible flow solvers based on a finite element discretization. Institute of Applied Mathematics (LS III), University of Dortmund, Vogelpothsweg 87, D-44227, Dortmund, Germany, 2006.